Alicja M Lacinska[1,2], Michael T Styles[1], Keith Bateman[1], Doris Wagner[1], Matthew R Hall[2], Charles Gowing[1] and Paul D Brown[2] 2016 *Acid-dissolution of antigorite, chrysotile and lizardite for ex situ carbon capture and storage by mineralisation.* Chemical Geology 437, 153-169

[1]British Geological Survey, Environmental Science Centre, Nicker Hill, Keyworth, Nottingham, NG12 5GG, United Kingdom. Email addresses: A.M. Lacinska alci@bgs.ac.uk (corresponding author), M.T. Styles mts@bgs.ac.uk, K. Bateman kba@bgs.ac.uk, D Wagner dwagner@bgs.ac.uk, C. Gowing cjbg@bgs.ac.uk,

[2]The University of Nottingham, University Park, Nottingham NG7 2RD, United Kingdom. Email addresses: P.D. Brown Paul.Brown@nottingham.ac.uk, M.R. Hall Matthew.Hall@nottingham.ac.uk

Authors version

ABSTRACT

Serpentine minerals serve as a Mg donor in carbon capture and storage by mineralisation (CCSM). The acid-treatment of nine comprehensively-examined serpentine polymorphs and polytypes, and the subsequent microanalysis of their post-test residues highlighted several aspects of great importance to the choice of the optimal feed material for CCSM. Compelling evidence for the non-uniformity of serpentine mineral performance was revealed, and the following order of increasing Mg extraction efficiency after three hours of acid-leaching was established: Al-bearing polygonal serpentine (<5%) ≤ Al-bearing lizardite 1T (≈5%) < antigorite (24-29%) < well-ordered lizardite $2H_1$ (≈65%) ≤ Al-poor lizardite 1T (≈68%) < chrysotile (≈70%) < poorly-ordered lizardite $2H_1$ (≈80%) < nanotubular chrysotile (≈85%).

It was recognised that the Mg extraction efficiency of the minerals depended greatly on the intrinsic properties of crystal structure, chemistry and rock microtexture. On this basis, antigorite and Al-bearing well-ordered lizardite were rejected as potential feedstock material whereas any chrysotile, non-aluminous, widely spaced lizardite and/or disordered serpentine were recommended.

The formation of peripheral siliceous layers, tens of microns thick, was not universal and depended greatly upon the intrinsic microtexture of the leached particles. This study provides the first comprehensive investigation of nine, carefully-selected serpentine minerals, covering most varieties and polytypes, under the same experimental conditions. We focused on material characterisation and the identification of the intrinsic properties of the minerals that affect particle's reactivity. It can therefore serve as a generic basis for any acid-based CCSM pre-treatment.

KEYWORDS

Serpentine minerals, mineral dissolution, CO_2 sequestration

INTRODUCTION

A recent Intergovernmental Panel on Climate Change (IPCC) report stated that human influence by CO_2 released from the burning of fossil fuels is clearly detrimental to the climate system [*Field et al.*, 2014]. One method proposed to alleviate CO_2 emissions is to sequester CO_2 permanently, *via* crystallographic capture, in the form of carbonate minerals, a process commonly termed carbon capture and storage by mineralisation (CCSM). In practice, CCSM involves the chemical reaction between CO_2 and divalent metal cations to form a new crystalline CO_2-bearing phase *i.e.* carbonate. Currently, two CCSM approaches are being considered: (i) *in situ* – whereby the CO_2 is injected underground into a suitable host-rock where it reacts to form carbonate [*Kelemen and Matter*, 2008; *Kelemen et al.*, 2011; *Matter and Kelemen*, 2009; *McGrail et al.*, 2014; *McGrail et al.*, 2006; *Schaef et al.*, 2011]; and (ii) *ex situ*, which involves carbonation of feedstock materials above-ground in a specifically designed CCSM plant [*Fagerlund et al.*, 2009; *Lackner et al.*, 1997; *Larachi et al.*, 2012; *Park and Fan*, 2004; *Sanna et al.*, 2014; *Sanna et al.*, 2013; *Wang and Maroto-Valer*, 2011a; b; *Werner et al.*, 2013]. Both host-rock for injection and feedstock materials must be widely available and contain large proportions of easily-extractable cations (*i.e.* Mg^{2+}, Ca^{2+}, Fe^{2+}) to form long-term stable carbonates. In practice, these will be Mg-rich rocks and previous work has shown that widely-available Mg-rich ultramafic rocks and serpentinites, in particular, are the most suitable feedstock materials (*Styles et al*., 2014; Bide *et al.,* 2014).

This paper reports on the acid-extraction of Mg from a broad selection of structurally and compositionally diverse serpentine minerals, potentially suitable for *ex situ* CCSM. Previous CCSM studies were performed under a wide range of physical and chemical conditions and mostly utilized only one type of serpentine, *e.g.* antigorite [*Krevor and Lackner*, 2011; *Maroto-Valer et al.*, 2004; *Park and Fan*, 2004 and references therein]; lizardite [*Daval et al.*, 2013; *Sanna et al.*, 2013; *Schulze et al.*, 2004; *Wolf et al.*, 2004]; or chrysotile [*Ryu et al.*, 2011; *Rozalen et al,* 2013]. Only a few have utilized two types of serpentine, lizardite and antigorite [*O'Connor et al.*, 2002; *Styles et al.*, 2014], and three or more have never been investigated under the same processing conditions, preventing a realistic comparison of the effects of mineral structure and composition on cation release; *i.e.* the first step in the CCSM process. In addition, the very small size of serpentine crystals results in mineralogical intergrowths on the millimetre to micrometre scale, making the separation of phase-pure material virtually impossible. Hence, all experimental studies reported to date have almost certainly utilized heterogeneous samples, which inevitably impacts the mineral dissolution and risks a misleading interpretation of data acquired if applied to CCSM technologies. Ideally, a comprehensive characterization of any naturally-sourced serpentine mineral should be performed

Authors version

prior to processing, data interpretation and process modelling, in order to gain improved understanding of the role of composition and microtexture on efficiency of reaction.

Here, we report on a systematic set of acid-extraction experiments of Mg from comprehensively-analysed serpentine minerals, the purest specimens we could isolate. We then discuss the geochemical and mineralogical factors at the micro-scale that cause significant differences in the efficiency of Mg extraction. In the light of the high applicability of serpentine minerals and serpentinites to CCSM technology, gaining improved understanding of their intrinsic functional performance is paramount.

BRIEF INTRODUCTION TO SERPENTINE MINERALS

The serpentine minerals are Mg-rich silicates with the general formula $Mg_3Si_2O_5(OH)_4$. They can exhibit the substitution of Si^{4+} cations by Al^{3+} or Fe^{3+}, and Mg^{2+} by Fe^{2+}, Mn^{2+}, Co^{2+} or Ni^{2+} [*Caruso and Chernosky*, 1979; *Fuchs et al.*, 1998; *Mellini and Zanazzi*, 1987; *Viti and Mellini*, 1997], with Al^{3+} being particularly important to their crystal chemistry-related reactivity [*Mellini*, 1982].

Serpentine minerals belong to the group of trioctahedral 1:1 layered silicates, consisting of one tetrahedral (T) and one octahedral (O) layer. The thickness of the T-layer is thinner than that of the O-layer, resulting is a subtle dimensional misfit between the two. This misfit can be reduced by substitutions in the tetrahedron, which in turn reduces interlayer strain and consequently enhances the mineral's stability [*Caruso and Chernosky*, 1979; *Mellini and Zanazzi*, 1987; *O'Hanley et al.*, 1989].

Further, the T and O-sheets are variably arranged and stacked one above another, giving rise to complex polymorphs and polytypes [*Bailey*, 1969]. These include flat-layer lizardite (including trigonal "T", hexagonal "H" and monoclinic "M" polytypes) (Figure 1a); tubular chrysotile (Figure 1b); wave-like antigorite (Figure 1c) [*Wicks and Whittaker*, 1975]; and polygonal [*Baronnet et al.*, 1994] (Figure 1d) and polyhedral serpentine [*Cressey et al.*, 2008].

The layers in the structure are linked by hydrogen bonds that form by pairing oxygen on the basal tetrahedral surface of one layer with an OH-group on the upper octahedral surface of the layer below. These bonds are generally long and weak but can be modified and strengthened by the degree of substitution. In particular, Al^{3+} in the tetrahedral layer promotes stronger hydrogen bonding and more stable structures [*Mellini*, 1982]. In specific polytypes of lizardite, *e.g.* two layer hexagonal $2H_1$, this bond exhibits lower strength due to a lengthening of the inter-layer distances [*Mellini and Zanazzi*, 1987].

Authors version

Figure 1 Schematic representation of serpentine minerals crystal structure, including: A) flat layer lizardite, B) tubular chrysotile, C) modulated antigorite [Mevel, 2003] and D) polygonal serpentine [adapted from Cressey et al., 2010].

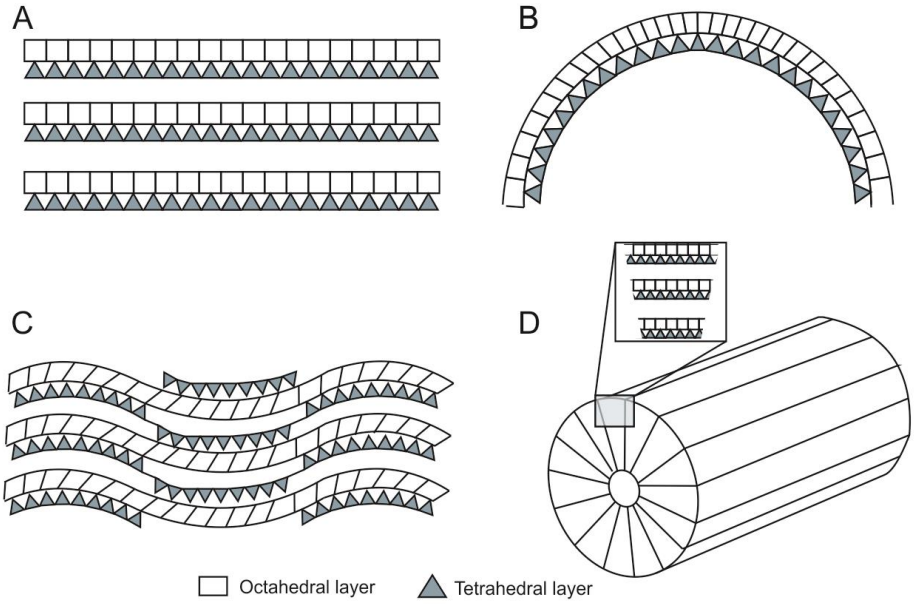

The serpentines are dominantly Mg-rich, containing approximately 40 wt% of MgO. In the context of *ex situ* CCSM, the Mg is released *via* a combination of pre-treatment processes, all of which ultimately lead to accelerated break-up of the crystal structure. The degree of structural break-up and hence the quantity of metal cations released, controls the extent of subsequent carbonation and thus the overall efficiency of this technological reaction. Previous research indicated that polymorphic and polytypic complexity of serpentine minerals may strongly influence mineral reactivity, but the underpinning reaction mechanisms are poorly understood [*O'Connor et al.*, 2002; *Styles et al.*, 2014; *Yoo et al.*, 2009 and references therein].

METHODS AND MATERIALS

Methods

X-ray diffraction was performed using a PANalytical X'Pert Pro series X-ray diffractometer, equipped with an X'Celerator detector, cobalt-target tube and generator operated at 45 kV and 40 mA, in Bragg-Brentano geometry. Scanning electron microscopy (SEM) was conducted using a LEO 435VP, variable pressure SEM and an FEI Quanta 600 environmental SEM (ESEM). Samples were analysed in the form of carbon sputter coated (≈ 25 nm thick) polished thin sections. Quantitative chemical analyses of the mineral phases were performed using an Oxford Instruments EDS system, following ASTM recommendations *(ASTM E1502-12a)*. Each SEM was operated under conditions of high vacuum (< 1.2 x 10^{-5} torr) at 20 kV accelerating voltage, with 10 mm (FEI SEM) and 19 mm (LEO SEM) optimal analytical working distances, and an X-ray detector take-off angle of 45°. For EDS analysis,

conditions of 1 nA beam current and 60 s acquisition times (spot mode) were used with the LEO SEM, whilst for the FEI Quanta 600 SEM the beam current values ranged from 1.5-7 nA, with 30 s acquisition time, giving ≈ 1 x 10^6 total X-ray counts. These experimental conditions of beam current, acquisition time and spot mode (rather than raster mode) provided optimal conditions for the analysis of major elements under conditions that prevented significant mineral de-hydroxylation under the focused electron beam. Transmission electron microscopy (TEM) investigations were performed using a JEOL 2100F TEM, with a high brightness, field emission gun (FEG) electron source. FTIR was performed using a BioRad Excalibur spectrometer on an optical bench containing a 60° dynamically aligned Michelson interferometer with ceramic infrared source, an air-cooled Deuterated Tri Glycine Sulfate (DTGS) detector and a potassium bromide beam splitter. KBr pressed discs were used as support medium for the analysis of powdered samples. The FTIR spectra were recorded in the 4000-400 cm^{-1} range with a spectral resolution of 2 cm^{-1}. Data was processed using Varian Resolution Pro software. X-ray fluorescence (XRF) spectroscopy was performed by PANalytical Ltd., Environmental Science Centre, Nottingham. 9 g of PANalytical pre-fused 66/34 $Li_2B_4O_7/LiBO_2$ flux was weighed into a 95/5 Pt/Au crucible and fused with 0.9000 g of sample powder at 1200°C. Loss of ignition (LOI) was determined after 1 h at 1050°C. The composition of the experimental leachates was determined using Perkin Elmer Optima 7300 DV (Dual View) Inductively Coupled Plasma - Atomic Emission Spectrometer with WinLab 32 for ICP (Version 5.5) software in the inorganic geochemistry laboratories. PHREEQC 3.2 geochemical code [*Parkhurst and Appelo*, 1999] was used to model the ionic speciation of experimental solutions, based on ionic concentrations measured in the leachates. This in combination with data from the Bureau de Recherches Géologiques et Minières (BRGM) database for phases of interest, was used to calculate the saturation indices (SI) of potential phases. Particle size distribution analysis was accomplished using an LS 13320 Laser Diffraction Particle Size Analyzer (Beckman Coulter), with a 5 mW diode laser, capable of measuring particle sizes in the range 0.017 to 2000 µm. Plots were prepared in "The R Project for Statistical Computing" using a code written by Dr B Rawlins (BGS). The N_2 BET specific surface area was measured using Micromeritics Gemini VI 2385 C physisorption system.

Materials

Nine samples of serpentine minerals and their acid-treated solid residues were investigated. The sample set included two antigorites, four lizardite–rich samples, two chrysotile-rich samples and one polygonal serpentine in a proto-serpentine matrix (Table 1). The proto-serpentine refers to an interstitial, "anhedral" poorly-crystalline, serpentine-like material, of composition similar to the adjacent polygonal serpentine, but exhibiting higher water content and thus being more beam

Authors version

sensitive. Most samples originated from veins to reduce the mineralogical and structural complexity, being distinct from the heterogeneous, serpentine-rich host-rock. The samples were crushed and hand-picked under a binocular microscope to remove magnetite and other clearly identifiable impurities, and analysed by XRD (Table 1). Some mineralogical heterogeneity was, however, unavoidable with three samples in particular, *i.e.* lizardite Liz1^{1T} containing ≈ 20% of chrysotile; lizardite Liz4^{1T} containing 10% of chlorite and 1 % of talc; and chrysotile Chr2 containing ≈ 11 % of calcite and trace amount of talc (Table 1). In an ideal laboratory dissolution experiment, one would use pure crystals but due to very fine mineral intergrowths in our samples this was not possible. However, the use of rock samples with intrinsic mineral heterogeneity better approximates an industrial process where large scale mineral separation might prove too expensive.

The samples were milled and sieved through a 250 µm mesh, considered appropriate for a possible industrial-scale process. Figure 2 summarises the particle morphologies and size distributions. Three dominant morphologies were observed: *i.e.* equant, which typified the lizardite samples and antigorite Ant1; elongate characteristic of the antigorite Ant2, polygonal serpentine and chrysotile samples; and platy, being characteristic of Liz4^{1T} that also contained chlorite and talc.

Table 1 Sample list, locality and composition. The mineralogical composition of the samples was obtained by XRD Rietveld Refinement analysis.

Sample Code	**Information on lizardite polytype**	**Locality of origin**	**Mineralogical composition**		
			Major (%)	**Minor (%)**	**Trace (%)**
Ant1		Pian del Re Monviso Massif, Italy	antigorite (99)		magnetite <1
Ant2		Unknown	antigorite (98.8)	lizardite (1.2)	
Liz1^{1T}	Trigonal 1 layer lizardite	Monte Fico, Elba Island, Italy	lizardite 1T (80)	chrysotile (20)	
Liz2^{2H1}	Hexagonal 2 layer lizardite	Gwendreath Quarry, Lizard Peninsula, UK	lizardite $2H_1$ (99.1)		chrysotile (0.1)
Liz3^{2H1}	Hexagonal 2 layer lizardite	Gwendreath Quarry, Lizard Peninsula, UK	lizardite $2H_1$ (98)	chrysotile (2)	
Liz4^{1T}	Trigonal 1 layer lizardite	Kennack Sands, Lizard Peninsula UK	lizardite 1T (89)	chlorite (10)	talc (1)
PS1	Polygonal serpentine with 1 layer lizardite in the polygons	Montecastelli, Tuscany, Italy	polygonal serpentine (60)	proto-serpentine (40)	
Chr1		Quarry NW of Bidya, UAE	chrysotile (94.7)	magnetite (4.3)	hematite (<1)
Chr2		New Amianthus Asbestos Mine, Transvaal region, South Africa	chrysotile (88.1)	calcite (11)	talc (<1)

Authors version

Figure 2 Secondary and backscattered electron images illustrating the diversity of particle sizes and shapes of the milled starting material. Corresponding particle size distribution curves are plotted as a function of % cumulative volume.

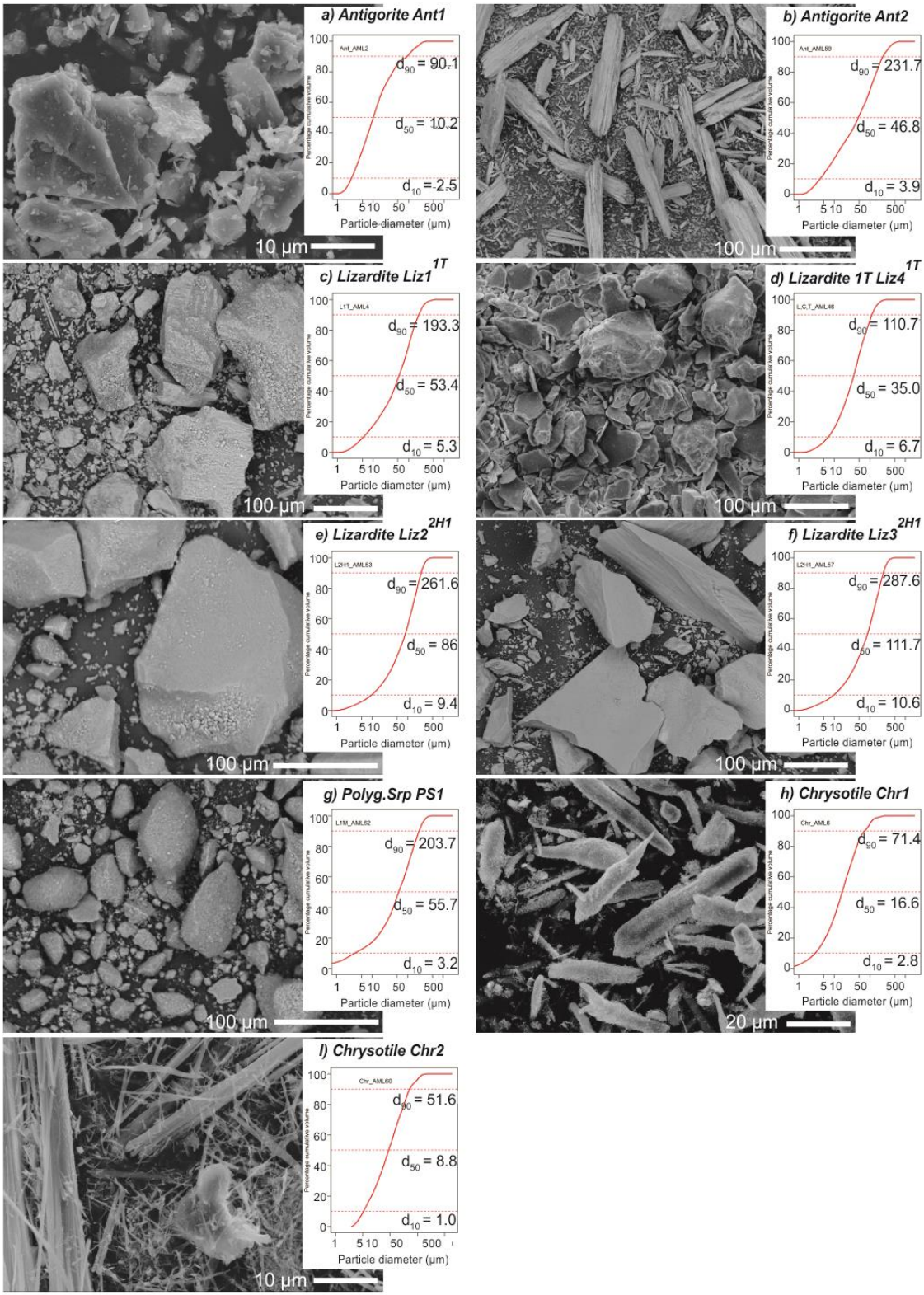

The powders contained texturally and compositionally heterogeneous particles. The term "microtexture" is used here to denote the within-particle mineral phase inter-growths. For example, some samples exhibited distinctive textural heterogeneity, with the lizardite-dominated samples (except Liz3^{2H1}) showing complex, fine-scale inter-growths of lizardite with interstitial chrysotile (with the interstices assigned to chrysotile based on the results of microanalysis Figure 3A and XRD) or numerous cross-cutting veins of "serpentine-like material"; being distinct from antigorite (as illustrated by Ant2, Figure 3B) and chrysotile that showed more textural homogeneity. It is noted that the chrysotile Chr1 sample was different slightly from the Chr2 sample, comprising more tightly inter-grown crystals. The Liz3^{2H1} sample showed evidence for micro-deformation, including shearing and brecciation that caused grain size reduction, annealing and re-crystallisation. This resulted in a largely homogeneous microtexture, with crystallographically and compositionally uniform particles. A distinctive microtexture was shown by sample PS1 that exhibited short-fibre polygonal serpentine set in an interstitial matrix of proto-serpentine (Figure 3C). Figure 3D shows the diffraction contrast TEM image of a cross-sectional view of an individual polygonal serpentine fibre with well-defined polygons.

Figure 3 Backscattered (A-C) and transmission electron images showing: A) texturally heterogeneous lizardite-dominated particle (Liz1) with lizardite 1T intergrown interstitially with chrysotile (lower BSE contrast); B) texturally homogeneous antigorite (Ant2) with tightly intergrown and aligned crystals; C) dual texture of short-fibre polygonal serpentine and a proto-serpentine matrix (lower BSE contrast) (PS1), D) Cross-axis HRTEM image of polygonal serpentine fibre (PS1). Image D, courtesy of M Fay and C Parmenter (Nottingham Nanotechnology and Nanoscience Centre).

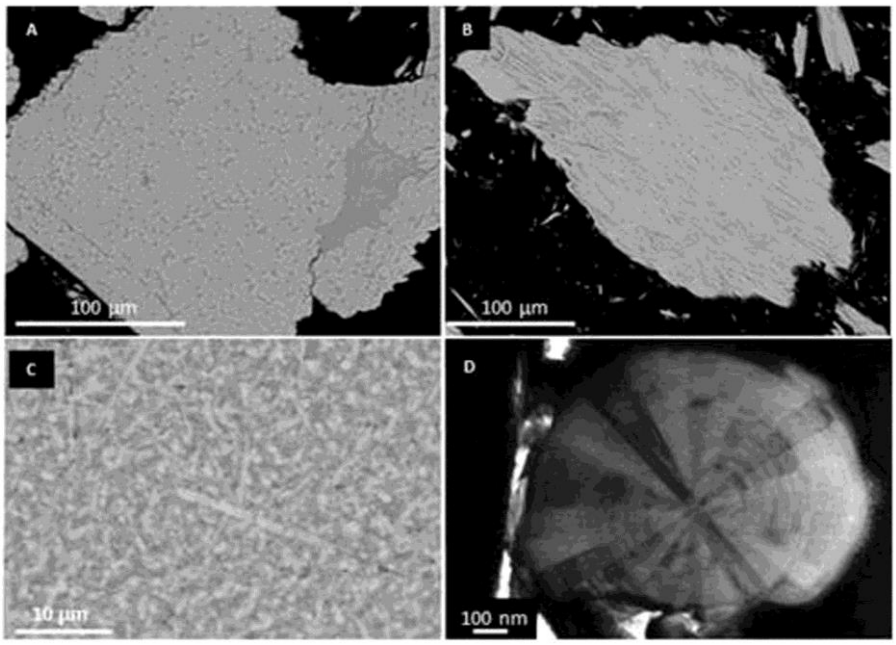

The bulk chemical composition of each sample is summarised in Table 2. As expected, most of the samples were dominated by SiO_2 and MgO, originating from the serpentine minerals. The XRF data was generally in good agreement with localised, quantitative SEM-EDS analyses of selected minerals

from the samples (Table 3), confirming the high levels of compositional homogeneity of the sample sets investigated. Due to the fine nature of the serpentine minerals, only samples with sufficiently large crystals were analysed quantitatively using EDS. The exceptions to this were Chr2 and Liz4^{1T} that exhibited significant mineralogical heterogeneity. Nevertheless, it is recognised that the XRF data can be treated as a good proxy for mineral composition and, as such, is utilised here. However, it should be stressed that this is not done routinely, and is only possible after careful consideration of all possible phases contributing to the chemical composition of a bulk sample.

It is noted that the samples exhibited significant variations in the concentrations of Al_2O_3 and Fe_2O_3 (representing the total Fe content, as reported routinely by XRF). Whilst the latter is likely related to variable amounts of iron oxides/oxyhydroxides, often associated with serpentine minerals, the Al_2O_3 signal was derived from the serpentine minerals themselves, with the exception of Liz4^{1T} that contained aluminous-chlorite. In particular, Liz1^{1T} and PS1 were the most-aluminous samples analysed here, containing up to 3.2 wt% Al_2O_3, as distinct from the remaining samples containing typically < 1 wt%.

Table 2 also shows (BET N_2) specific surface area (SSA) values, utilised in the calculations of reaction rates. The spread of the values from relatively low in the antigorite samples Ant1 and Ant2 (2.9 and 3.6 m^2/g) and the lizardite 1T sample Liz1 to moderate for lizardite $2H_1$ Liz2 and Liz3 (16.1 and 16.6 m^2/g) and relatively high for chrysotile samples Chr1 and Chr2 and the heterogeneous sample of Liz4 (29.4 m^2/g) reflect the increase of mesopore volume. Further investigation on accurate pore size distribution is required to assign the pore volume to microporous (< 2nm diameter, IUPAC 1994) and/or mesoporous (2-10 nm diameter, IUPAC 1994).

Authors version

Table 2 Starting materials used, summarising bulk composition (XRF), loss of ignition (LOI) and the specific surface area (SSA). The Al_2O_3 content in Liz4^{1T} is mostly related to the presence of Al-chlorite, whilst the significant amount of CaO in Chr2 reflects the presence of calcite (in cross-cutting vein) in the starting material that has also affected the low Total of this particular sample.

	Ant1	*Ant2*	*Liz1^{1T}*	*Liz2^{2H1}*	*Liz3^{2H1}*	*Liz4^{1T}*	*PS1*	*Chr1*	*Chr2*
	wt%								
SiO_2	**41.58**	**43.7**	**39.99**	**42.39**	**42.65**	**43.09**	**40.06**	**38.26**	**37.77**
TiO_2	<0.01	<0.01	<0.01	<0.01	<0.01	0.16	<0.01	<0.01	<0.01
Al_2O_3	**1.54**	**0.29**	**2.93**	**0.89**	**0.2**	**2.8**	**3.17**	**0.28**	**0.12**
Fe_2O_{3t}	6.63	4.15	4.28	1.85	1.04	1.36	3.29	11.19	1.82
Mn_3O_4	0.09	0.13	0.04	0.03	0.03	0.12	0.04	0.08	0.26
MgO	**39.14**	**40.82**	**40.34**	**42.25**	**42.08**	**37.85**	**40.97**	**38.06**	**34.64**
CaO	<0.01	<0.01	0.14	0.01	0.02	0.05	0.02	0.13	7.96
Cr_2O_3	0.3	0.01	0.01	<0.01	0.01	0.02	<0.01	<0.01	<0.01
NiO	0.22	0.09	0.04	0.2	0.21	0.19	<0.01	0.07	<0.01
Total	89.51	89.19	87.77	87.62	86.24	87.18	87.55	88.07	82.58
LOI	12.1	12.52	13.2	13.94	14.46	14.93	13.6	13.23	14.36
SSA (m^2/g) (±1%)	2.9	3.6	6.1	16.1	16.6	29.4	10.2	17.3	27.2

Authors version

Table 3 Quantitative SEM EDS analysis of selected samples. The difference of 100%-total was assigned to structural water present in the serpentine minerals.

	Ant1	*Ant2*	*Liz1*^{1T}	*Liz2*^{2H1}	*Liz3*^{2H1}
	wt%				
MgO	38.8	38.6	39.4	42.1	41.2
Al_2O_3	1.4	0.3	3.1	0.9	0.4
SiO_2	44.1	45.0	41.7	44.3	44.8
FeO	3.5	4.6	3.9	1.3	1.4
NiO	0.2	0.1	-	-	0.3
Total	88.0	88.6	88.1	88.6	88.1

**2% errors may apply to values ≥15wt%, increasing with decreasing element concentration*.

Authors version

Experimental Procedure

The experimental conditions (Table 4) are adapted from Wang and Maroto-Valer (*2011*), who used recyclable ammonium salts for integrated CO_2 capture and mineral carbonation. Accordingly, nine powdered serpentine mineral samples were leached in solution of 1.4 M ammonium bisulphate at 70°C and ambient pressure, for a maximum of three hours. The pH of the staring solution was ≤0.54, and the evolution of pH during the experiment is presented in Table 5. A subtle variation of the initial pH values is related to five, individually prepared batches of experimental solution. Each powder sample was split into four 10 g sub-samples and poured into separate HDPE bottles filled with 200 ml of the pre-heated to 70°C acid and placed on a rotation mixer (6 rpm). For each sample set, the leaching experiments were stopped after 30, 60, 120 and 180 minutes. This allowed both liquid and solid reaction products to be collected systematically for analysis to determine time-dependent compositional and textural transformations.

Table 4 Summary of experimental conditions.

Powder fraction	Sample mass (g)	Solution	Initial pH	Solution Volume (ml)	P	T°C	Duration (min)
<250 µm	10 (±0.01)	1.4 M NH_4HSO_4	≤0.54	200 (±2)	Ambient	70 (±5)	30 60 120 180

RESULTS

Efficiency of Mg extraction from serpentine minerals

Mg was extracted from the set of structurally and compositionally-different serpentine minerals using concentrated acid. Extraction efficiencies Mg^{EE} (%) were calculated from Mg concentrations in the 30, 60, 120 or 180 minute solid reaction residues (C_x), and compared to the Mg concentration in an unreacted sample (C_t), following:

$$Mg^{EE}\ (\%) = (C_x*100)/C_t$$

with Figure 4 illustrating the development of Mg^{EE} as a function of time. Hereafter, the term Mg^{EE} is used to refer to extraction efficiency values after 3 h of leaching. It is clear that amongst all the samples studied, the highest Mg^{EE} of nearly 85% was obtained for Chr2 followed by $Liz3^{2H1}$ with *ca.* 80% Mg^{EE}. Significantly lower reactivities were observed for antigorite (Ant1 and Ant2), aluminous $Liz1^{1T}$ and aluminous PS1 with values of Mg^{EE} ~5% and below for the latter two. It is noted that the values for aluminous lizardite and polygonal serpentine represent the reactivity of the polytype corrected for mineral impurity *i.e.* 20% of chrysotile and ≈ 40% of proto-serpentine respectively. The

Authors version

correction involved a simple subtraction and was possible after detailed microanalysis of the reaction products that revealed that both polytypes remained virtually unchanged whilst the chrysotile and proto-serpentine exhibited pervasive alteration in Liz1^{1T} and PS1, respectively.

The clear grouping of chrysotile, Al-poor lizardite and lizardite 2H$_1$ with the highest Mg^{EE}, being distinct from antigorite and aluminous serpentine with significantly lower Mg^{EE}, provides compelling evidence for extraction efficiency being dependent strongly on the type of serpentine mineral, *i.e.* its structure and crystal chemistry. Overall, the following trend for increasing Mg^{EE} was observed:

Al-bearing polygonal serpentine (<5%) ≤ Al-bearing lizardite 1T (≈5%) < antigorite (24-29%) < well-crystalline lizardite 2H$_1$ (≈65%) ≤ Al-poor lizardite 1T (≈68%) < chrysotile (≈70%) < poorly-ordered lizardite 2H$_1$ (≈80%) < nanotubular chrysotile (≈85%).

Figure 4 Mg^{EE} (%) from structurally different serpentine minerals, showing high efficiency of chrysotile, Al-poor and two-layer polytype of lizardite and low efficiency for antigorite, Al-lizardite 1T and Al-polygonal serpentine. It is noted that the data points for PS1 are tentative only (hence faint line), due to uncertainty related to proto-serpentine content. The graph was prepared based on XRF data obtained from starting materials and four solid reaction residues. The error bars show possible 5% variation.

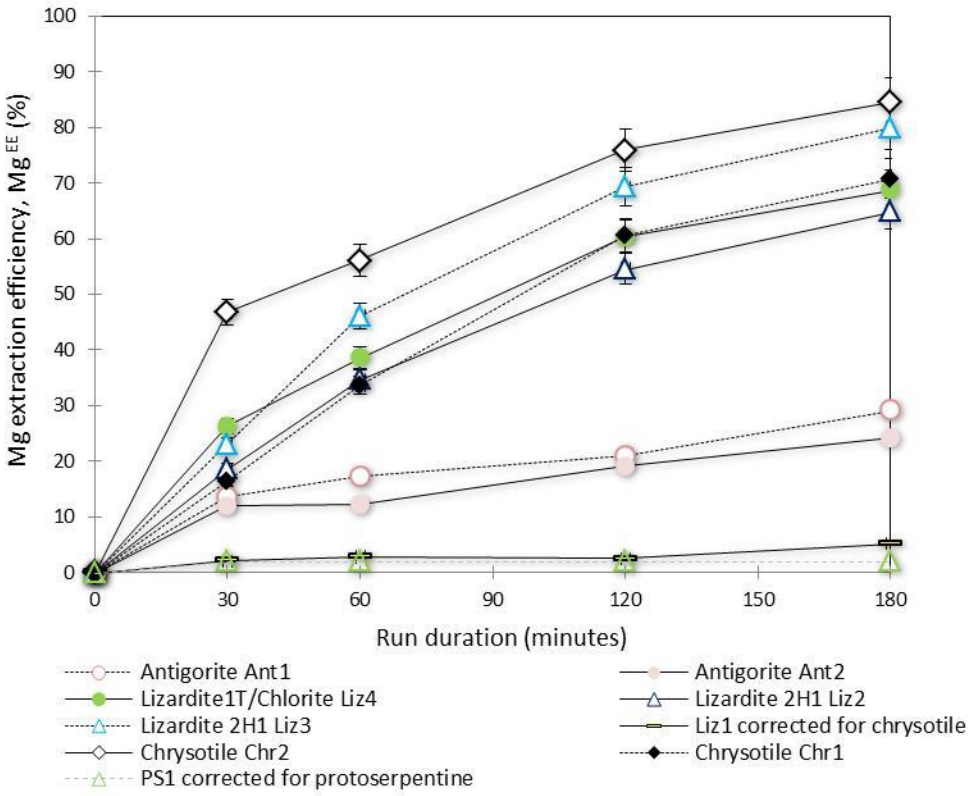

The rate of serpentine dissolution

The dissolution rate *(R)* of each serpentine mineral was calculated using the concentration of Mg in the leachate solution, following the method modified after Brantley *et al* (2008),

$$R = (\frac{V}{SSA} * \frac{dC}{dt})/n$$

where V is the volume of solution used (l); SSA is the specific BET (N_2) surface area (m^2/g) of the starting material; *dC/dt* is the change in elemental concentration (mol) with time (s); and *n* is a coefficient calculated from mineral stoichiometry, assuming that all Mg in the bulk was associated with the serpentine minerals (XRF data, Table 2).

Figure 5 The log rate ($logR^{Mg}$) of mineral dissolution as a function of time: A) showing antigorite Ant1, Ant2, and chrysotile samples Chr1, Ch2; B) showing lizardite samples $Liz1^{1T}$, $Liz2^{2H1}$, $Liz3^{2H1}$, $Liz4^{1T}$ and the polygonal serpentine sample PS1. The rates were calculated based on the concentrations of Mg in the leached solutions and normalised for changes in mineral stoichiometry. It is clear that lizardite $2H_1$ and chrysotile exhibited higher values of $logR^{Mg}$ than antigorite and $Liz1^{1T}$, PS1; largely corresponding to the degree of mineral dissolution illustrated by the Mg^{EE}.

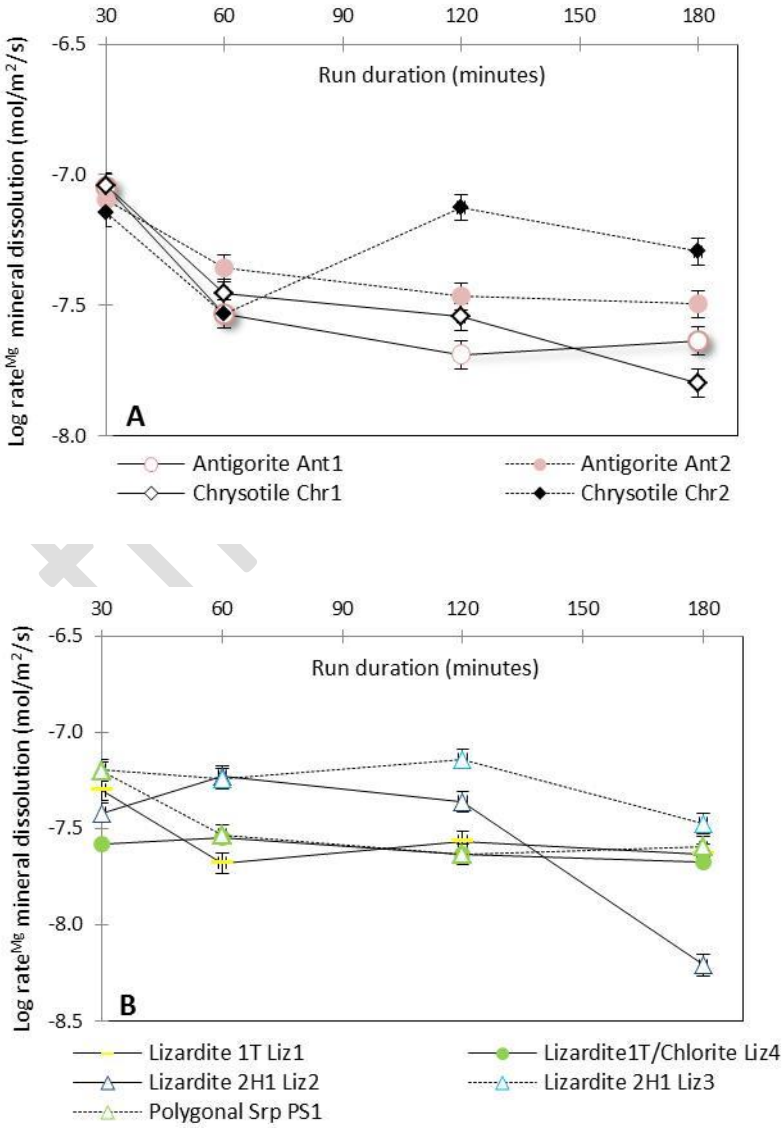

The rate of mineral dissolution values (Figure 5 A, B and Table 5) ranged from $logR^{Mg}$ *ca.* -7 mol/m^2/s for Ant1 to $logR^{Mg}$ *ca.* -7.6 mol/m^2/s for Liz4^{1T} after the first 30 minutes of reaction; with a general decreasing trend over the duration of all the experimental runs. The exceptions were Liz41T and Liz22H1 samples that exhibited a subtle logRMg increase towards the 60 and 120-minute time interval, respectively, followed by a decrease. Similarly, Liz11T and Chr2 showed logRMg increase towards the 120-minute time point of the reaction. These cases might reflect a combination of the fast initial dissolution rates due to the preferential attack of fines and a time-delay in the activation of reactive surfaces within the particles, resulting from chemical, textural and/or structural obstructions. Also, the noticeable drop in $logR^{Mg}$ for the lizardite $2H_1$ sample may be related to the formation of a siliceous reaction front, previously reported as passivating mineral dissolution *[Daval et al, 2011],* and discussed below.

The $logR^{Mg}$ values obtained in this study of *ca*. -7 to -8.2 mol/m^2/s at pH < 1, were significantly higher than those reported for antigorite [*Critelli et al.*, *2015*], lizardite [*Daval et al.*, *2013*] and chrysotile [*Thom et al.*, *2013*] with logR values *ca.* -11 mol/m^2/s at pH ≈ 2. This substantial difference may be related to a combination of different pH of solutions used and a dissimilarity of temperature conditions, with 70°C utilised here compared to 25°C, 27°C and ~ 22°C, respectively, in the referenced studies. This is consistent with the Arrhenius equation showing that the rate of a thermally-accelerated reaction might double for every 10°C rise in temperature. Furthermore, the experimental procedure reported here involved materials sieved only to a maximum size rather than a narrow size range, *i.e.* containing particle < 250 µm in diameter, including rapidly reacting fines compared to the abovementioned studies where the fines were ultrasonically removed [*Daval et al.*, *2013; Critelli et al.*, *2015*].

Table 5 presents a summary of experimental and calculated data, including the evolution of pH with time, measured at 20°C and calculated at 70°C (PHREEQC 3.2). It is noted that the use of several batches of experimental fluid caused minor differences in the initial pH; however the reader should focus on the trend of pH evolution rather than small variation in the absolute values. The trend is clear and shows pH increase over time related to mineral dissolution buffering.

Authors version

Table 5 Summary of experimental and calculated data.

	Liquids data								Solids data
	Duration (min)	pH measured at 20°C	pH calc. at 70°C	[Mg] mg/l	[Si] mg/l	[Mg]/[Si]	log (R) ^{Mg}	log (R) ^{Si}	^Mg EE %
Ant 1		[&]0.24init.		4.7	<0.056				
	30	0.12	0.44	1270.0	145.2	8.74	-7.05	-7.94	13.68
	60	0.15	0.21	1660.0	158.6	10.47	-7.53	-8.96	17.38
	120	0.22	0.3	2165.0	185.2	11.69	-7.69	-8.91	21.00
	180	0.23	0.31	2650.0	195.6	13.55	-7.64	-9.28	29.20
Ant 2		0.38init.							
	30	0.16	0.22	1510.0	85.5	17.67	-7.10	-8.30	11.91
	60	0.16	0.22	2344.0	126.6	18.51	-7.36	-8.64	12.25
	120	-0.03	0	3518.0	173.5	20.28	-7.47	-8.89	19.11
	180	0.23	0.23	4533.0	190.3	23.82	-7.50	-9.35	24.25
Liz 1^{1T}		0.54init.							
	30	0.35	0.47	1594.0	112.3	14.19	-7.30	-8.39	2.0
	60	0.36	0.48	2239.0	149.1	15.01	-7.68	-8.88	2.0
	120	0.46	0.65	3856.0	213.0	18.11	-7.56	-8.97	2.0
	180	0.46	0.65	5151.0	232.6	22.14	-7.63	-9.49	5.0
Liz 2^{2H1}		0.24init.							
	30	0.45	0.45	3035.0	116.0	26.16	-7.42	-8.84	18.57
	60	0.63	0.95	6727.0	201.7	33.36	-7.23	-9.02	34.73
	120	0.82	1.25	10383.0	241.7	42.96	-7.36	-9.70	54.57
	180	0.93	1.41	10777.0	210.9	51.10	-8.21	*NA	64.94
Liz 3^{2H1}		0.38init.							
	30	0.54	0.45	4913.0	152.4	32.24	-7.19	-8.77	22.95
	60	0.70	0.61	7873.0	187.7	41.94	-7.24	-9.46	46.14
	120	1.02	0.92	12000.0	220.6	54.39	-7.14	-9.84	69.29
	180	1.12	1.01	13237.0	207.1	63.92	-7.47	NA	80.02
Liz 4^{1T}		0.54init.							
	30	0.45	0.63	2855.0	154.2	18.51	-7.58	-8.90	26.31
	60	0.58	0.86	5366.0	202.8	26.46	-7.54	-9.42	38.65
	120	0.75	1.15	7836.0	205.5	38.13	-7.63	-10.93	60.38
	180	0.84	1.29	9536.0	217.1	43.92	-7.68	-10.27	68.84
PS 1		0.44init.							
	30	0.60	0.5	3377.2	182.2	18.53	-7.20	-8.47	2.0
	60	0.65	0.55	4713.5	217.3	21.69	-7.53	-9.16	2.0
	120	0.73	0.63	6393.8	232.3	27.52	-7.63	-9.77	2.0
	180	0.80	0.7	7897.3	226.2	34.91	-7.60	NA	2.0
Chr 1		0.22init.							
	30	0.54	0.44	4768.0	264.2	18.05	-7.04	-8.38	16.29
	60	0.71	0.61	6458.0	260.7	24.77	-7.45	NA	33.61
	120	0.71	0.62	8466.0	205.8	41.14	-7.54	NA	60.55
	180	0.81	0.72	10029.0	204.3	49.10	-7.80	NA	70.79
Chr 2		0.22init.							
	30	0.78	0.66	4052.0	227.2	17.83	-7.15	-8.48	46.78
	60	0.88	0.77	5397.0	199.1	27.11	-7.53	NA	56.10
	120	1.09	0.99	9040.0	178.4	50.68	-7.13	NA	75.83
	180	1.17	1.06	10631.0	175.2	60.68	-7.29	NA	84.57

**NA – represents samples where the precipitation rate exceeded the dissolution rate, most probably being related to precipitation of amorphous silica. [&]The variations in the initial pH values ±0.32 are due to the use of five individually prepared batches of solution. These values are only given here to show the trend of pH evolution as a function of time. The three cases of Ant, Ant2 and Liz1^{1T}, where the experimental pH is lower than the starting pH (albeit increasing with time) are the samples with least reaction occurred. ^The Mg^{EE} for Liz1^{1T} and PS1 show values normalised for mineral heterogeneity, please see details in the text, and represent the efficiency for Al-bearing lizardite 1T and polygonal serpentine respectively.*

Authors version

Congruency of dissolution and secondary phases

Figure 6 illustrates the time evolution of Mg and Si concentration (mg/l) in the leachates of Ant1, Liz1^{1T}, Liz2^{2H1} and Chr2, with approximately one order of magnitude more Mg being released than Si in all cases. The starting serpentine-rich material contained roughly equal amounts of Mg and Si, and their distinctively unequal release into solution, also manifested by the measured Mg/Si ratio (Table 5), is consistent with a process of incongruent dissolution. Further, the rates of mineral dissolution based the concentration of Si is noticeably lower than that based on Mg (Table 5), collectively indicating preferential release of Mg to the solution. This can be explained by the different reactivity of octahedral (Mg) and tetrahedral (Si) sheets in serpentine minerals, and favoured dissolution of the octahedral brucite sheet at low pH conditions *(Park and Fan, 2004).*

Figure 6 Time evolution of Mg and Si concentration in the leachates of Ant1, Liz1^{1T}, Liz2^{2H1} and Chr2; all plots clearly indicate an incongruent release of the two cations into the solution.

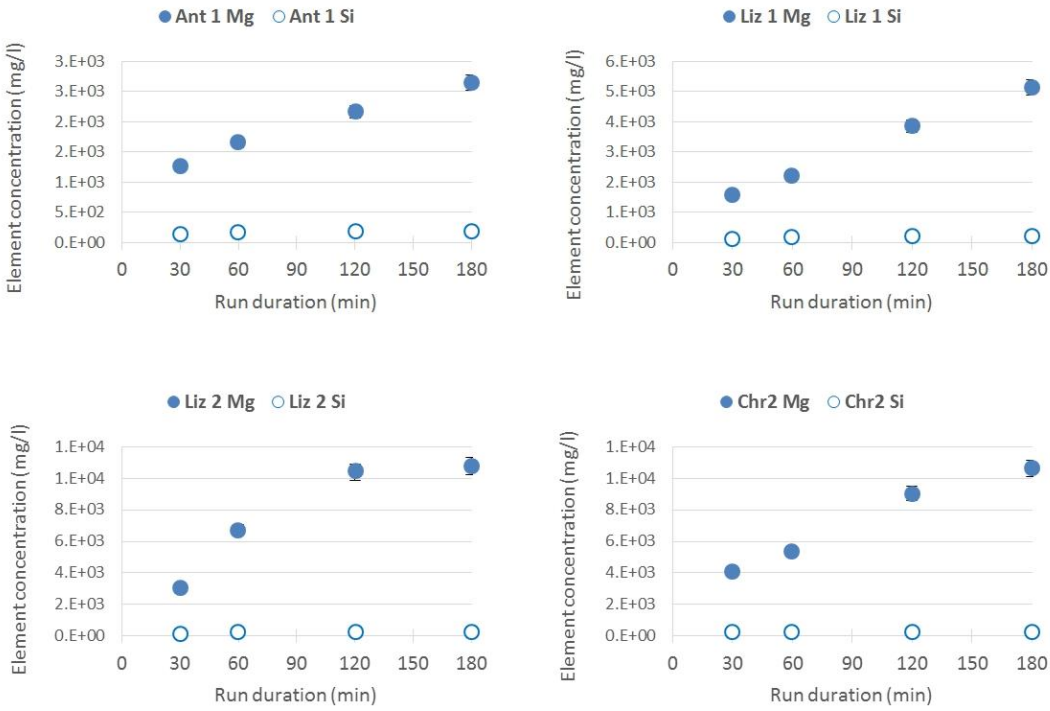

The incongruent dissolution of serpentine minerals in the presence of NH_4HSO_4 resulted in siliceous residuum, *i.e.* Mg-leached solid product and trace amounts of hydrated sulphate minerals, including boussingaultite ($(NH_4)_2Mg(SO_4)_2{\cdot}6H_2O$) and hexahydrite ($MgSO_4{\cdot}6H_2O$), the latter two being a side-effect of ammonium bisulphate use. Geochemical modelling using PHREEQC 3.2 (*Parkhurst and Appelo*, 1999) showed that the experimental solutions were far from equilibrium with respect to serpentine minerals, as expected, with saturation index (SI) values for antigorite ranging from *ca.* -

773 to -553, lizardite and chrysotile ranging from *ca*. -27 to -41 (Table 6). The general unification of SI values for the latter two mineral types is surprising, particularly in the light of their significantly different extent of dissolution. This might be related to the limited availability of thermodynamic data for serpentine minerals, resulting in utilisation of one set of lizardite data only, without accounting for structural, *i.e.* the polytypic complexity of this mineral.

The solutions were saturated with respect to amorphous silica (Table 6). Due to the lack of thermodynamic data for boussingaultite, this mineral could not be considered in the modelling. The solutions were undersaturated with respect to hexahydrite, with SI varying from -1.5 to -2.9, however trace amounts of this mineral was observed in the $Liz1^{1T}$ residuum.

Furthermore, the speciation-saturation calculations suggested the possibility of secondary pyrite (FeS_2) in solutions of $Liz3^{2H1}$, PS1 and chrysotile samples, and secondary eskolaite (Cr_2O_3) in Ant1; however it is anticipated that eskolaite would form at higher P-T conditions than those used in this study and hence is not considered a realistic precipitate here [*Logvinova et al.*, 2008]. The high saturation index calculated for pyrite also requires further investigation because microanalysis of the solid residues did not reveal any evidence for its presence. It also should be emphasised that the geochemical modelling using PHREEQC may provide less reliable results for high ionic strength solutions, such as those used in this study and hence, it is important to interpret the output data in conjunction with complementary information from the experiment products, *e.g.* the microanalysis data from the solid reaction residues as done in this study.

Authors version

Table 6 Saturation indices of serpentine minerals and secondary phases calculated using PHREEQC 3.2 [*Parkhurst and Appelo*, 1999]

Mineral Phase	Time	Ant1	Ant2	Liz1^{1T}	Liz2^{2H1}	Liz3^{2H1}	Liz4^{1T}	PS1	Chr1	Chr2
		Saturation Index (SI)								
Antigorite	30	-657.8	-572.2							
	60	-572.5	-556.9							
	120	-558.8	-563.6							
	180	-552.8	-772.7							
Lizardite	30			-35.2	-41.1	-33.5	-33.3	-33.6		
	60			-34.4	-30.4	-31.9	-31.1	-32.7		
	120			-32.5	-28.2	-29.5	-29.2	-31.8		
	180			-32.1	-27.5	-28.9	-28.2	-31.1		
Chrysotile	30								-33.6	-32.8
	60								-32.4	-31.9
	120								-32.2	-30.3
	180								-31.4	-29.4
Amorphous silica	30	0.3	0.3	0.1	0.3	0.2	0.2	0.2	0.4	0.3
	60	0.2	0.2	0.1	0.3	0.2	0.3	0.3	0.4	0.3
	120	0.2	0.2	0.3	0.4	0.3	0.3	0.3	0.3	0.2
	180	0.3	0.3	0.3	0.3	0.3	0.3	0.3	0.3	0.2
Hexahydrite	30	-2.6	-2.6	-2.8	-1.9	-2.2	-2.5	-2.3	-2.2	-2.1
	60	-2.9	-2.9	-2.6	-2	-1.9	-2.1	-2.1	-1.9	-1.9
	120	-2.8	-2.8	-2.3	-1.7	-1.5	-1.8	-1.9	-1.8	-1.6
	180	-2.7	-2.7	-2.2	-1.5	-1.4	-1.7	-1.8	-1.7	-1.5

Authors version

Micro-scale phase transformation

The extent of leaching-induced transformation of serpentine, *i.e.* Mg-silicate to silica-dominated material, varied from sample to sample. A combination of factors, including the size fraction of the particles and their compositional and textural arrangements, *i.e.* the distribution of structurally and chemically-different minerals and their degree of intergrowth, may account for this.

The initially homogeneous samples of antigorite remained largely unchanged for the coarsest size fraction ($\gtrsim$ 50 µm), whilst the finest size fraction became pervasively-leached. Backscattered electron (BSE) observations revealed that leaching mostly affected < 5 µm sized particles, with complete Mg-removal from $\lesssim$ 1 µm particles. This spread of leaching responses resulted in an overall Mg^{EE} for antigorite samples of 24 - 29%.

In contrast, the chrysotile samples showed a great extent of mineralogical transformation, with the smallest particles, and the nanotubular Chr2 in particular, exhibiting nearly-complete transformation to siliceous material, being consistent with their high Mg^{EE} of 70 – 85%. Less pervasive alteration occurred for sample Chr1, with the coarsest fraction being only partially Mg-leached. It is noted that the original calcite in sample Chr2 dissolved during the experiment, and Ca reacted with solution to form gypsum, $CaSO_2x2H_2O$ (< 20 µm euhedral crystals).

Neither antigorite nor chrysotile showed evidence for either Mg-depleted, Si-enriched reaction fronts at a scale of few to tens of microns or localised, preferentially-altered sectors, as distinct from the lizardite samples described in detailed in the following section.

The most diverse range of phase transformations was observed in the lizardite samples which corresponded well with their respective Mg^{EE} values. The transformations are illustrated by representative BSE images and associated X-ray element distribution maps for samples $Liz1^{1T}$ and PS1, respectively in Figure 7.

Authors version

Figure 7 Backscattered electron images of representative acid-leached particles of serpentine minerals (180 min solid residuum), and associated X-ray element distribution maps, showing: A) Liz1^{1T} with preferentially leached serpentine, tentatively assigned to chrysotile ([a]) and intact aluminous-lizardite ([b]); B) Liz2^{2H1} with deeply Mg-leached zones, now siliceous residuum as illustrated in the EDS X-ray spectrum 2; C) Liz3^{2H1} with leached micro-scale layer texture with deeply Mg-leached reaction rim and partially altered particles core. Note the sharp contact between the leached and partially leached zones; D) PS1 with subtly Mg-leached rim, and generally a roughly uniform transformation; E) high magnification of particle "D", showing a dual nature of this sample with polygonal serpentine, represented by bright BSE laths in a matrix of proto-serpentine. The associated maps clearly indicate that the matrix is Mg-depleted and Si-enriched, proving that its leaching contributed most to the Mg^{EE} as plotted in Figure 4. The scale bar, unless specified, corresponds to 100 µm, showing all the particles are roughly the same size.

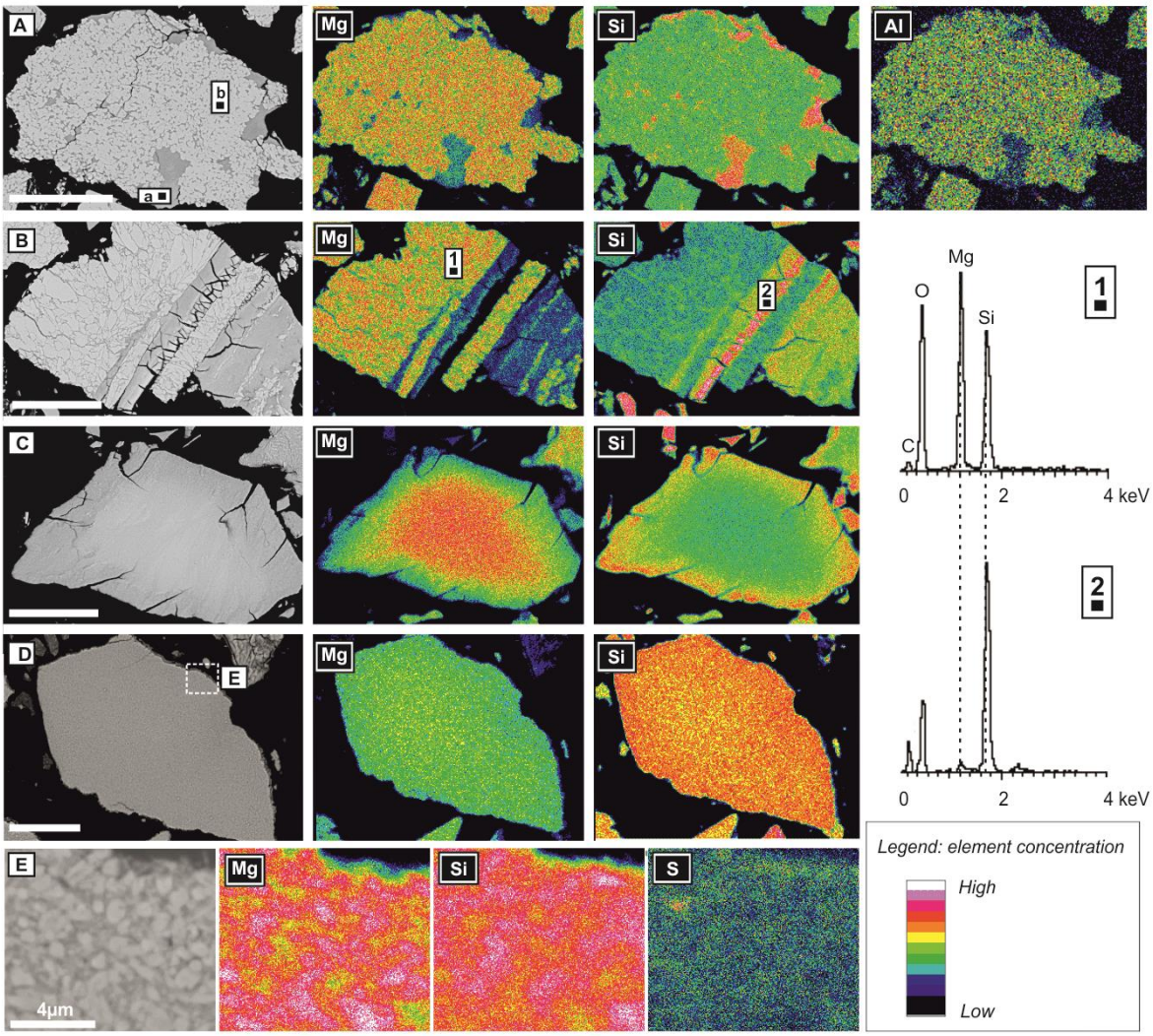

The Liz1^{1T} with low Mg^{EE} exhibited only localised alteration (Figure 7A), with leached zones in the particle being interstitial to the aluminous-lizardite 1T. These leached zones matched closely the distribution of chrysotile in the starting material, whilst the aluminous-lizardite 1T remained largely intact. Localised alteration was evident also for Liz2^{2H1} (Figure 7B), originally identified as a two layer hexagonal polytype $2H_1$. The starting material was texturally-heterogeneous with well-developed crystals and interstitial or locally confined zones (veins) of "anhedral" serpentine-like material (characterised by lower mean atomic number, compared to adjacent crystals). This textural duality was enhanced during prolonged acid-leaching, with greater Mg-extraction being observed from the

serpentine-like material. The other lizardite $2H_1$ sample (Liz3) was more-homogeneous texturally and generally less-crystalline than Liz2, as indicated by peak broadening in the associated XRD pattern in contrast to the sharp diffraction peaks for $Liz2^{2H1}$ (Lacinska, PhD thesis). Sample $Liz3^{2H1}$ exhibited a very high Mg^{EE} of 80% with a largely uniform pattern of phase transformations, showing concentric Mg-depletion and siliceous layer formation, commonly termed leached layers [*Hellmann et al, 1990; Hellmann et al.*, 2003; *Teir et al.*, 2007; *Weissbart and Rimstidt*, 2000 and references therein]. SEM-EDS data demonstrated that the amount of Mg within the $Liz3^{2H1}$ core material was similar to that in the starting material, *i.e.* ≈ 40 wt%, whilst changing gradually into the Si-rich layer from ≈ 35 wt% close to the Si layer-core boundary to ≈ 20 wt% at the particle edge. The layer-core boundary was uneven and coincided with the termination of inward-tapering cracks (Figure 7C).

The alteration patterns in a polymineralic sample of $Liz4^{1T}$ containing lizardite 1T, *ca.* 10% of chlorite and <1% of talc were complex. It was found that neither talc nor chlorite showed any significant evidence for dissolution and almost intact crystals of both were present in the leached residuum. The lizardite 1T-dominated particles exhibited preferential Mg-depletion along zones of "anhedral serpentine-like material", similar to those observed in $Liz2^{2H1}$. Again, the presence of original textural complexity of finely inter-grown serpentine phases resulted in preferential leaching manifested by the presence of prominent leaching-resistant zones adjacent to deeply-leached residuum.

A distinctive set of alteration patterns was observed for the PS1 sample with sectors of lizardite 1M set in a proto-serpentine matrix. As illustrated in Figure 7D, the prolonged exposure to acid resulted in a narrow (<30 µm thick), slightly Mg-depleted Si-enriched layer but a general absence of a well-defined rim-core boundary, being distinct from $Liz3^{2H1}$. The SEM-EDS analysis showed that the amount of MgO oscillated between 25-35 wt% throughout the entire particle, the oscillation being resultant from the inherited inhomogeneity of proto and well-crystalline polygonal serpentine. Analysis under high magnification (Figure 7E) revealed that the nanotubular, short-fibre crystals of polygonal serpentine remained virtually intact (returning higher MgO values). The proto-serpentine matrix was pervasively leached, resulting in significant Mg-depletion leaving an interstitial siliceous material. The intrinsic duality of phases in the starting sample controlled the degree of reactive fluid ingress, and consequently the extent and distribution of Mg-depleted regions.

It was noted that mineral heterogeneity (*e.g.* the presence of calcite in original Chr2) combined with the use of NH_4HSO_4 as a solvent created artifact in these experiments. Boussingaultite ($(NH_4)_2Mg(SO_4)_2{\cdot}6H_2O$) and gypsum were formed. The formation of boussingaultite in particular, is potentially problematic due to its potential to capture Mg. Although it was a trace component of the solid residues and appears to have formed from adsorbed surface liquid during drying of the

Authors version

samples, the data presented here for leaching efficiency is based on analysis of these solids, and the exact values of Mg^{EE} may be associated with some uncertainty, albeit minor.

Structural modification

The acid leaching and extraction of variable amounts of Mg resulted in a significant modification to the crystal structure of the affected serpentines. The degree of modification varied according to the amount of Mg extracted and an example of extreme modification is shown by Chr2. Figure 8 shows a TEM image of a bundle of acid-leached chrysotile fibres. The associated EDS spectrum and diffused rings of selected area electron diffraction pattern (SAED), clearly indicate that the 180-minute residuum is silica-dominated and amorphous.

Figure 8 TEM image of a bundle of acid-leached chrysotile (180 min Chr2) fibres and corresponding EDS spectrum and SAED pattern, indicating that the leaching residuum is silica-dominated and amorphous. Trace amounts of Mg and S were also detected, originating from the mineral and solution, respectively; whilst the prominent Cu and C peaks in the EDS spectrum are from Cu grid and C-based film, holding the sample.

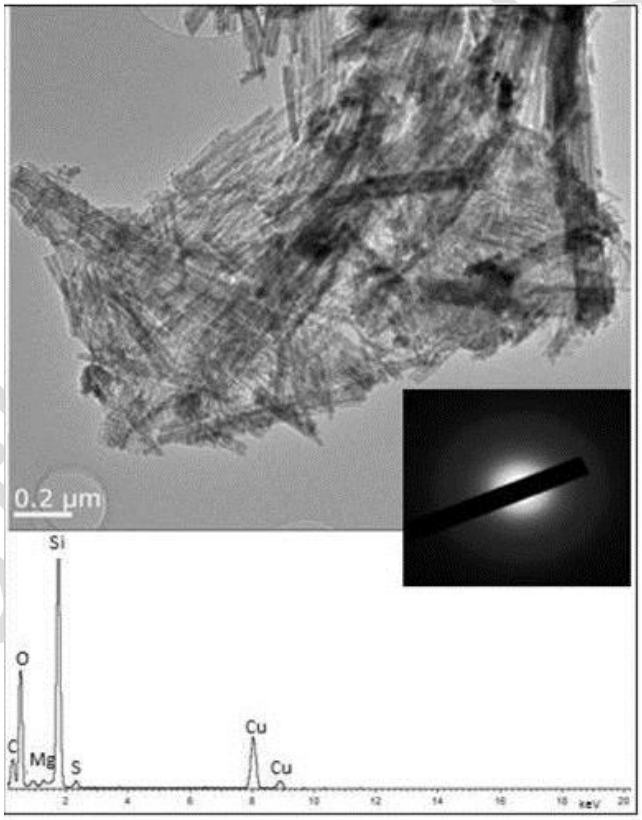

A progressive modification of a crystal structure was demonstrated by the changes in IR bands corresponding to specific bonds in the crystal lattice. Here, sets of FTIR spectra are shown for Ant1, $Liz1^{1T}$ and Chr2 being representative of all samples analysed in this study (Figure 9). The most prominent structural modifications were observed in two spectral regions related to the lattice

vibrations and generally involved changes in a relative intensity of peaks and/or the formation of new shoulders/peaks:

(i) Basal and apical Si-O bonds, at 983 cm^{-1} and 1066 cm^{-1} in antigorite; 950 cm^{-1} and 1080 cm^{-1} in lizardite 1T, and 965 cm^{-1} to 1088 cm^{-1} in chrysotile, respectively. A general decrease in the "basal Si-O peak" intensity was observed and attributed to a time-dependent transformation within SiO_4 tetrahedra and preferential breakage of weaker, basal Si-O bonds. This is most prominently shown in Chr2 that exhibited a near-complete loss of the basal Si-O peak after 180 minutes leaching. This high degree of structural deformation of chrysotile, in comparison with lizardite and antigorite, is in agreement with the high Mg^{EE} of this specific serpentine polymorph.

Structural modifications in the region of apical Si-O were related to general peak broadening and the presence of a new absorption band at *ca.* 1083cm^{-1}, previously attributed to amorphous silica [*Madejova*, 2003]. A low intensity peak at *ca.* 1143 cm^{-1} in Ant1 (Figure 9, yellow arrow) and a distinctive shoulder in $Liz1^{1T}$ were observed in the 120 and 180 minutes residues. The resolution of this peak was reported previously to be sensitive to the degree of quartz crystallinity, and a well-defined peak/shoulder was attributed to a well-crystalline phase (*Shoval el al, 1991*). In Chr2, the quartz-related peak/shoulder at *ca.* 1145 cm^{-1} was not observed and the leaching resulted in formation of largely amorphous siliceous residuum, also confirmed by a low intensity peak at *ca.* 800 cm^{-1} [*Madejova*, 2003]. This peak was apparent for Chr2 and $Liz1^{1T}$ but less prominent for Ant1. In particular, in $Liz1^{1T}$ starting material, the low intensity peak at *ca.* 800 cm^{-1} (marked by black-filled arrow) could be assigned to tetrahedrally coordinated ferric iron [*Fuchs et al.*, 1998]

The modified Si-O related peaks overlapped also with bands corresponding to secondary gypsum and/or boussingaultite, and a distinctive peak at 1102 cm^{-1} (180 minutes residuum) probably related to either amorphous silica (opal in [*Farmer*, 1974]) or to stretching vibrations of SO_4 tetrahedra [*Liu et al.*, 2009] originating from secondary minerals was observed. The presence of gypsum was also manifested by two peaks previously assigned to O-H bending vibration modes at *ca.* 1682 cm^{-1} and 1619 cm^{-1} [*Liu et al.*, 2009].

(ii) inner OH bonded to Mg cations in the octahedral position, at *ca.* 3676 cm^{-1} for antigorite, 3684 cm^{-1} for lizardite, and 3690 cm^{-1} for chrysotile (*Viti and Mellini, 1997*). The greatest decrease in the relative intensity with time was observed for Chr2, in agreement with previous observations of high Mg^{EE}. Equally, the low Mg^{EE} in Ant1 and $Liz1^{1T}$ was represented by the presence of a residual, but still well-defined peak in this spectral region. Further, the depletion of Mg in the chrysotile structure is confirmed by progressive extinction of bands at 604 and 558 cm^{-1},

Authors version

corresponding to the vibrations of Mg-O (out of plane bending mode of Mg-octahedra) and δ(OH) *(Rozalen et al 2013).*

Other changes observed in the reaction residues were related to the formation of boussingaultite $(NH_4)_2Mg(SO_4)_2{\cdot}6H_2O$, whilst a series of low intensity peaks observed between 1435 cm^{-1} and 1470 cm^{-1} were attributed to bending vibrations of NH_4 bonds [*Culka et al.*, 2009]. The SO_4 stretching vibrations in boussingaultite occurred at *ca.* 980 cm^{-1} to 1133 cm^{-1} and overlapped with Si-O vibrations from serpentine minerals. Broad bands at *ca.* 1630 cm^{-1} and 3300 - 3440 cm^{-1} were probably related to H_2O, either in the crystal structure or in form of moisture adsorbed onto the particles [*Farmer*, 1974; *Madejova*, 2003]. Peaks at *ca.* 1430 cm^{-1} and 887 cm^{-1} in the chrysotile starting material were attributed to the presence of calcite [*Adler and Kerr*, 1963].

Authors version

Figure 9 FTIR spectra of (a) Ant1 (b) Liz1[1T] and (c) Chr2 and associated reaction residues; reflecting the time dependent structural modifications that occurred during acid leaching. The blue arrows correspond to secondary boussingaultite, the yellow arrows indicate a low intensity peak attributable to quartz, and the orange arrows indicate a peak corresponding to amorphous silica.

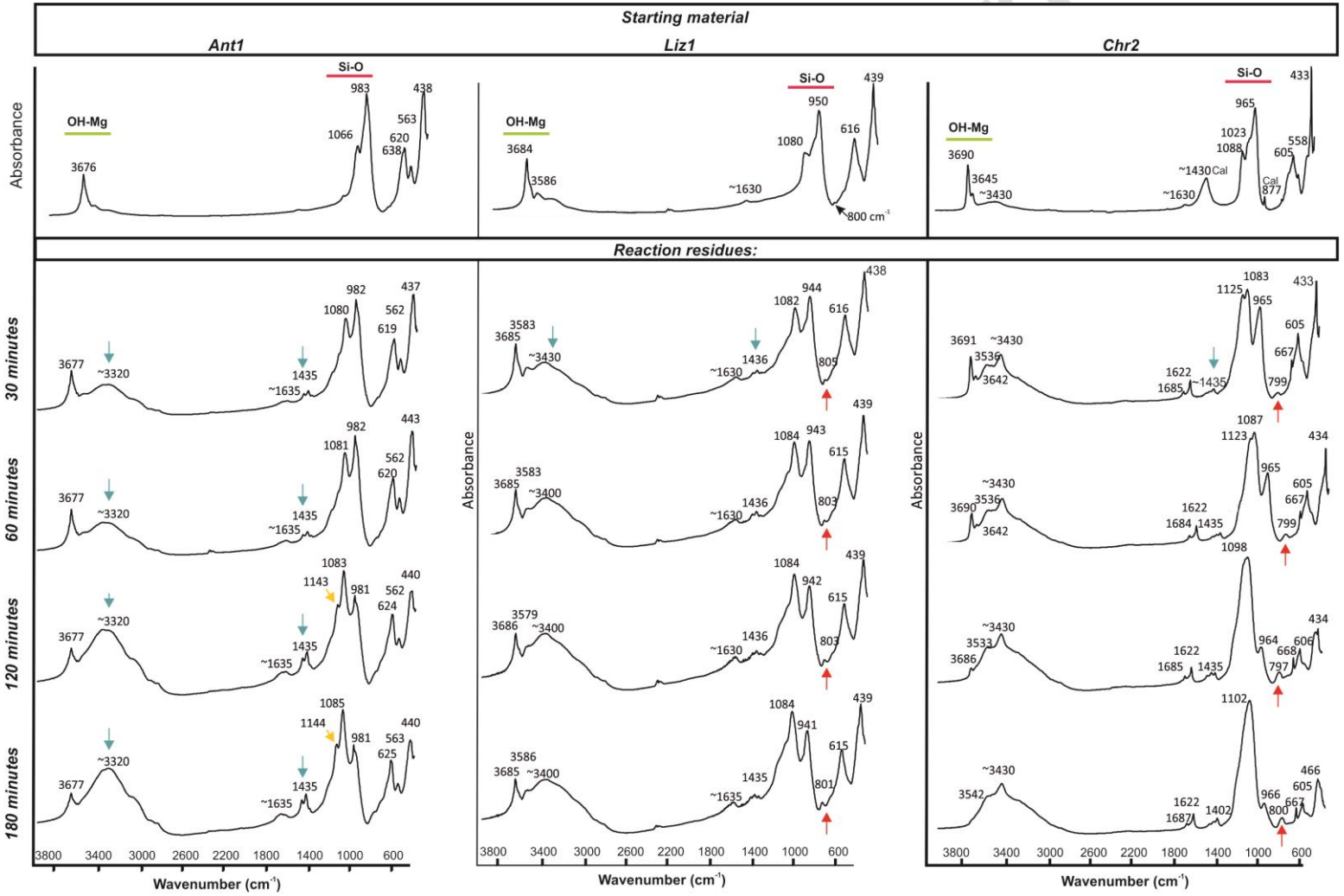

DISCUSSION

The combined results from microanalysis of the solid residues and chemistry of the leachates provide compelling evidence for the non-uniform reactivity of serpentine minerals under acid leaching conditions. It is evident that there is a strong influence of the starting material crystal structure, chemistry and rock microtexture on the extent of Mg^{EE}. The following order of increasing Mg^{EE}, consistent across the polymorph groups, has been determined as:

Al-bearing polygonal serpentine (< 5%) ≤ Al-bearing lizardite 1T (≈ 5%) < antigorite (24-29%) < lizardite $2H_1$ well-crystalline (≈ 65%) ≤ Al-poor lizardite 1T (≈ 68%) < chrysotile (≈ 70%) < lizardite $2H_1$ poorly-crystalline (≈ 80%) < nanotubular chrysotile (≈ 85%).

Comprehensive understanding of how rock structure, chemistry and microtexture inter-play, when subjected to physical and chemical processing, is paramount to evaluate material's efficiency and performance in a CCSM system.

Effect of rock microtexture on tens of microns thick, siliceous layer formation

In an ideal scenario, dissolution experiments should be performed on a single type of homogeneous mineral. However, some minerals, such as serpentine, only occur as finely inter-grown crystalline aggregates, usually with minor impurities of other minerals. When milled into fine powder, they cannot be regarded as consisting of small single crystals, but as fragments of rock with specific, intrinsic microtexture.

The rock microtexture provides fine-scale porosity, on the micro- or nano-scale depending on the size of the original features that serves as pathways for reactive fluid ingress and hence is an important parameter when assessing fluid-rock interactions. Microtexture generally encompasses: (i) the spatial distribution of morphologically and compositionally varied crystals; (ii) the number and dimension of veins and fractures; and (iii) micro-deformation, *e.g.* crystal elongation and thinning, resulting from shearing.

The geochemical data suggested incongruent dissolution of the serpentine minerals-rich particles and preferential release of Mg into the solution, with the potential for development of Mg-depleted siliceous layers at the peripheral zones of the affected particles. The micro-scale investigation revealed that only two samples leached for three hours at pH <1 contained tens of microns thick siliceous layers, *i.e.* indistinct in PS1 and distinct in $Liz3^{2H1}$. Further study is required to determine the presence of nano-scale layers in the remaining samples, as previously observed by others on single

Authors version

crystals of albite, labradorite, or wollastonite [*Hellmann et al, 1990; Hellmann et al.*, 2003, *Ruiz-Agudo et al.,* 2012]; as well as to investigate the incipient layers formation at a shorter leaching time.

Figure 10 shows a schematic representation of a conceptual model for the siliceous layer formation through $2H^+ \rightarrow Mg^{2+}$ exchange, based on microanalysis of the two samples. Particle (a) is a composite of randomly oriented, frequently hollow, short-fibre crystals of polygonal serpentine and a less-crystalline proto-serpentine matrix (sample PS1). After acid leaching, the evidence showed that dissolution was preferential, with the matrix being affected more strongly. A subtle Mg-depleted, Si-enriched layer (marked with arrow) was observed at the edge of the particle, as revealed by the element distribution maps and quantitative microanalysis line profiles (*e.g.* Figure 10A, line profile X1-X2 originated from PS1, Figure 7D). The scatter of data, being slightly more pronounced for MgO, was attributed to the textural duality of the sample. The presence of trace amounts of sulphur, originating from the acid, throughout the leached-particles (Figure 7E) supports a pervasive influx of reactive fluid deep into the particle. It is likely that progressive leaching of the proto-serpentine matrix created secondary micro-porosity, with well inter-connected pathways for the reactive fluid and promoted uniform transport of H^+ into and Mg out of the particle. Consequently, this resulted in a roughly uniform leaching of the entire particle. Particle "B" was almost entirely composed of lizardite $2H_1$ and exhibited a highly homogeneous microtexture (*e.g.* $Liz3^{2H1}$). The microtexture was uniform and largely fluid impermeable, hence the most prominent leaching occurred in the outermost zone. Acid-rock interactions resulted in a deeply Mg-leached, siliceous layer that became brittle and developed distinctive, inward-tapering cracks (Figure 7C) due to significant removal of cations and consequent structural collapse and volume change. A gradual but distinct interface between the siliceous layer and the core of the particle developed (Figure 10B), as demonstrated by low-angle parabolic, SEM-EDS measured, MgO and SiO_2 line profiles Y1-Y2 (Figure 10).

Authors version

Figure 10 Schematic representation of a conceptual model for siliceous layer formation through $2H^+ \rightarrow Mg^{2+}$ exchange in two types of lizardite-rich particles (≈ 400 µm across), A) before and after leaching particle with elongate crystals of polygonal serpentine set in proto-serpentine matrix, collectively representing a dual micro-texture and B) before and after, distinctively deformed but texturally homogeneous particle of generally poorly-crystalline lizardite $2H_1$ (Liz3). The associated measured (EDS) element distribution line profiles show roughly uniform chemical gradient in PS1 (with the fluctuation corresponding to the compositional duality of the sample) and sharper gradient between the siliceous layer and the core of the particles in Liz3. The faint straight lines on the element distribution profiles represent the oxide composition of the starting material, blue for SiO_2 and red for MgO.

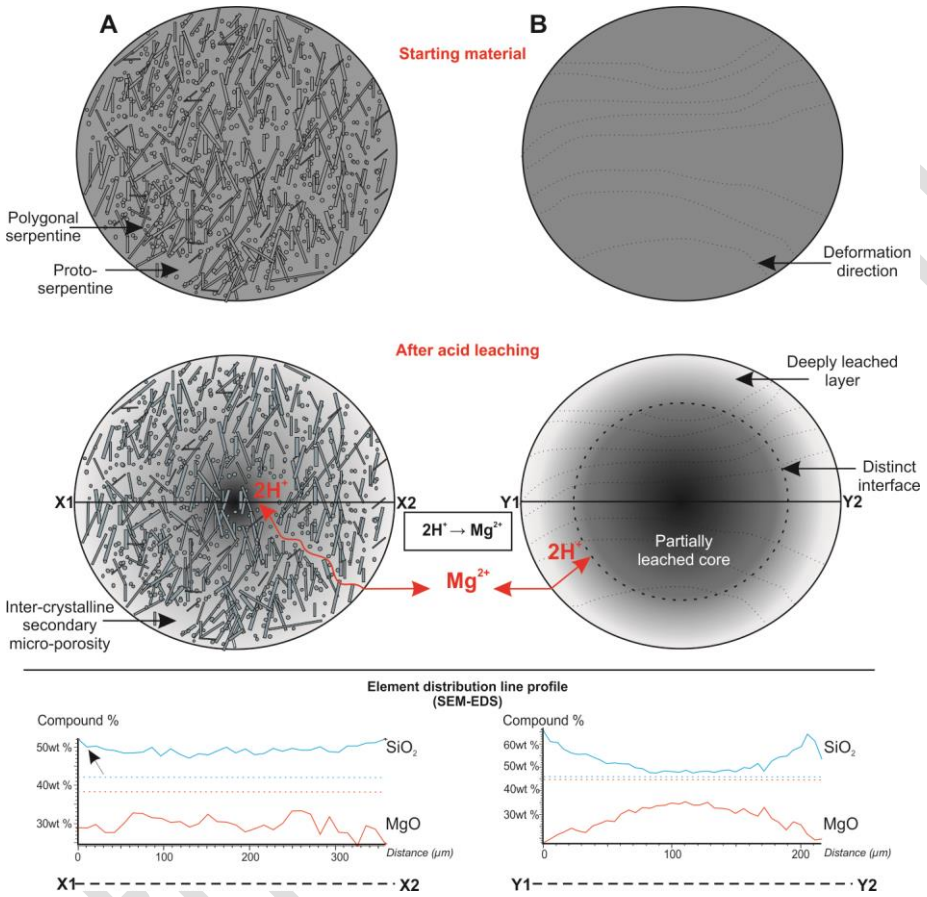

Even though the same acid leaching conditions were applied to this set of serpentine minerals, a well-defined siliceous layer was observed only for $Liz3^{2H1}$ and less strongly for PS1, being in accordance with Daval *et al* (2011) and Schott *et al* (2012), who suggested that the formation of a leached layer is not universal and dependent on many factors including mineral structure and time of the reaction. Our study provides further evidence that at a scale of tens of microns and pH<1 as investigated here, the layer formation is facilitated and greatly affected by rock microtexture. It is emphasized that the particles in the starting powder, unless they are equal or finer than the mineral crystals, are treated as fragments of rocks with intrinsic textural heterogeneity manifested by intergrowths of minerals or cross-cutting veins and dislocations. The importance of textural heterogeneity was also noted by Hellmann *et al.* [1990] in a study of leached layer formation in albite. Accordingly, the formation of a siliceous layer in a dual, intrinsically micro-permeable system containing highly reacting proto-serpentine matrix, PS1, did not necessarily affect the extent of

dissolution, being distinct from texturally more homogeneous particles, where the layer was impermeable, consequently inhibiting the ingress of acid and limiting the dissolution of the particle core, as shown for sample Liz3^{2H1}. Further, in texturally heterogeneous systems, such as observed in Liz1^{1T}, no siliceous layers were observed at the scale investigated here. Instead, deeply leached interstices and veins, corresponding to the less acid-resistant chrysotile, were observed and these appear to have maintained access for the acid.

It is considered that leached layers might form through: (i) *incongruent dissolution* and exchange of cations in the outermost zone of a mineral with hydrogen from solution, leading to preferential removal of cations showing weaker bonding with oxygen [*Weissbart and Rimstidt, 2000; Schott et al., 2012*]; and/or (ii) *interface coupled dissolution/precipitation*, with bond-breaking, elemental release and re-precipitation at the advancing fluid-mineral interface [*Hellmann et al.*, 2003; *Putnis*, 2009; *Ruiz-Agudo et al.*, 2012]. Although, the siliceous layers observed in this study are not *sensu stricto* leached layers, *i.e.* developed at a single crystal-scale as described by others, they might represent an extreme case of their growth at longer reaction times, very low pH<1 and in texturally heterogeneous materials. Due to their potential for reaction inhibition *via* fluid passivation, a comprehensive understanding of the layers formation and distribution will have a great impact on the design of experimental conditions for CCSM technology. Although their formation mechanism requires further research at the nano-scale and shorter reaction times, the amorphous state of the Si-rich residuum, as indicated by SAED patterns and FTIR spectra; the presence of residual Mg in the siliceous layers; the apparent incongruency of dissolution with respect to the Mg and Si concentrations in the leachates over time (Figure 6); the saturation of experimental solutions with respect to amorphous silica, SI ≈ 0.3 (Table 6) (PHREEQC 3.2 [*Parkhurst and Appelo*, 1999]), and finally the decreasing amount of Si in the solution with time in Liz2^{2H1}, Liz3^{2H1}, Chr1 and Chr2 indicating that silica precipitation exceeded dissolution (Table 5), collectively suggest that at pH < 1, as used in this study, the tens of microns thick siliceous layers might have formed *via* a combination of incongruent dissolution and silica re-precipitation, overgrowing the residual material in the secondary micro-porosity. In this context, it is noted that the dissolution of powder with a wide range of particle sizes, constitutes a dynamic system, whereby the finest particles dissolve preferentially and provide silica in solution that in turn, undergoes re-precipitation as amorphous material in the micro-pores within the larger, partially leached particles.

Irrespective of the mechanism of siliceous layer formation, the two examples presented here are considered representative of two fundamental processes that occur at the mineral-fluid interface:

Authors version

i.e. molecular diffusion and surface reaction [*Murphy et al.*, 1989]. Fast reaction at the surface results in the development of a depletion zone below the solid surface and the formation of a siliceous layer, as observed for Liz3^{2H1}; whilst the prevalence of molecular diffusion leads to roughly uniform leaching of the entire particle [*Schott et al.*, 2009], as observed in PS1 sample.

The effect of mineral chemistry

An inversely proportional relationship between Mg^{EE} and the presence of structural Al^{3+} within these minerals is shown in Figure 11, indicating that the greater the $Al^{3+} \rightarrow Si^{4+}$ substitution, the stronger the crystal structure and the lower the tendency to break-up and release cations. This is in a good agreement with the proposal for enhanced mineral-structural stability through a reduction of interlayer misfit [*Caruso and Chernosky*, 1979; *Mellini and Zanazzi*, 1987; *O'Hanley et al.*, 1989]. Although not investigated here in detail, the crystal order might also be increased by substitution of other trivalent cations in both tetrahedral and octahedral positions, including Fe^{3+}. This is related to increasing linkage by H bonding from layer to layer [*Mellini and Viti, 1994*].

Figure 11 Mg^{EE} as a function of Al_2O_3 content in the starting material. Three samples were plotted after appropriate correction, *i.e.* Liz1^{1T}_corrected fro chrysotile; Liz4^{1T}_corrected for Al-chlorite and PS1_corrected for proto-serpentine. An inversely proportional relationship between the Al_2O_3 content and Mg^{EE} is apparent for all, but antigorite samples.

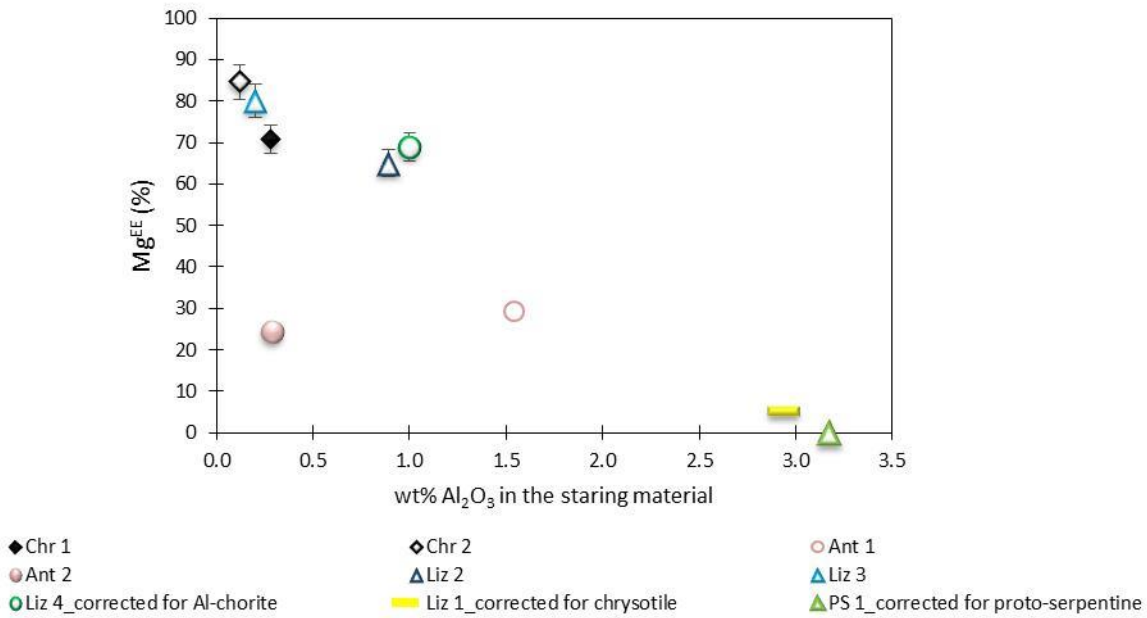

It is noted that, in mineralogically homogenous samples, *e.g.* Liz2^{2H1}, the Al^{3+} level was assigned predominantly to tetrahedral positions, substituting for Si^{4+}. This substitution is exemplified by lizardite 1T (Liz1^{1T}) with formula unit: $(Mg_{2.72}\ Fe^{total}_{0.15}\ Al_{0.11})_{\Sigma 2.98}\ (Si_{1.94}\ Al_{0.06})_{\Sigma 2}\ O_5(OH)_4$, as indicated by

quantitative EDS analysis. A portion of the Al^{3+} balances the slightly undercharged Si^{4+} tetrahedron (1.94 atoms per formula unit *[apfu]*), with the remaining amount placed in octahedral positions along with Mg and Fe. As indicated by the FTIR spectroscopy, trace amount of Fe^{3+} may be present in the tetrahedral position along with Al^{3+} and Si^{4+}; being in a general agreement with previous results on a mineral from the same locality analysed by Mössbauer spectroscopy [*Fuchs et al, 1998*].

Further, to provide for a more realistic, mineral-specific performance, as a function of Al_2O_3, three samples were corrected for intrinsic-mineral heterogeneity, *i.e.* aluminous mineral content other than serpentine. Accordingly, $Liz1^{1T}$ was corrected for 20% of chrysotile, returning a Mg^{EE} for Al-lizardite 1T only; $Liz4^{1T}$ was corrected for Al-rich chlorite (contributing to high bulk Al_2O_3levels) and plotted based on the content of Al in the lizardite 1T, on the basis of SEM-EDS analysis; whilst PS1 was adjusted for ≈ 40% of the proto-serpentine matrix, returning a tentative value (with uncertainty related to the exact amount of proto-serpentine present) for Mg^{EE} associated with the Al-polygonal serpentine only. It should be emphasized that this correction was only possible following detailed microanalysis of the materials before and after experimentation. Antigorite, in particular, with a general low leachability, was less affected by the Al^{3+} content, as explained below.

The effect of crystal structure

This study highlighted the great importance of serpentine mineral structural diversity on the extent of mineral dissolution, with consistently low Mg^{EE} from antigorite samples compared to considerably higher Mg^{EE} from chrysotile and lizardite $2H_1$ samples. The serpentine minerals, whilst being compositionally and structurally similar, exhibit significant differences in the details of their crystal structures. This structural diversity stems from a subtle dimensional misfit between the tetrahedral and octahedral layers that can be alleviated by some adjustment in the chemical substitutions, as shown earlier, and/or layer arrangement [*Wicks and Whittaker*, 1975]. Accordingly, in antigorite, a modulated structure resulting from periodic inversion of the tetrahedral layers attached to the concave side of octahedral layers results in a complex three-dimensional network of chemical bonds extending throughout the entire crystal [*Capitani and Mellini*, 2004]. As a consequence, a so called "antigorite chemical cement" forms that proved resistant to acid-attack, leading to an overall low to moderate Mg^{EE}.

In chrysotile, the interlayer misfit is compensated by layer curvature that leads to a tubular crystal structure with tetrahedral sheet on the inside and octahedral sheet on the outside of the tube [*Capitani and Mellini*, 2004]. The strong curvature and tubular morphology result in higher inter-crystalline strain and a defective lattice, that in turn, lead to faster bond breaking and

Authors version

dehydroxylation [*Gualtieri et al.*, 2012]. In addition, the inner surface of the nanotubes provides additional reactive surface, enhancing further the overall reaction, as observed for the nanotubular Chr2 sample with ~ 85% Mg^{EE}. The lower, ~ 70%, Mg^{EE} obtained for the Chr1 chrysotile sample was probably related to the specimen microtexture. Specifically, the crystals were densely packed and interlocked, producing a felted microtexture that caused a subtle increase in acid-resistance. The starting powder sample was also slightly coarser, with d_{50} of 16.6 µm, compared to d_{50} = 8.8 µm for Chr2.

In lizardite, the flat layers exhibit a wide range of stacking arrangements, manifested by subtle layer shifts and rotations, giving rise to polytypes [*Bailey, 1969*]. It is known that even very minor structural modifications affect bond lengths from structure to structure [*Mellini and Zanazzi, 1987*], impacting on strength. In this context, the interlayer basal spacing is longer in lizardite $2H_1$ compared to lizardite 1T [*Mellini and Zanazzi, 1987*], resulting in weaker bonding and consequently higher probability of structural break-up and cation release.

Another important aspect of crystal structure, displaying apparent impact on mineral reactivity, is the degree of structural order. It has been shown that a less-ordered proto-serpentine in the PS1 sample, albeit being Al-rich, was Mg-leached to a great extent. Similarly, the lower structural order of $Liz3^{2H1}$ with deformation–induced defects and high surface-strain energy greatly improved the leachability of this material, resulting in higher Mg^{EE}, being distinct from well-crystalline $Liz2^{2H1}$.

Summary

This study has highlighted several important factors influencing the Mg-leaching properties of serpentine that are of great importance to the choice of optimal feedstock material for *ex situ* CCSM. Firstly, compelling evidence for the non-uniformity of serpentine mineral performance has been provided. Their dissolution was greatly dependent on mineral intrinsic properties, such as crystal structure and chemistry. Importantly, the inter-play of the two, together with rock microtexture explains the relatively poor performance of antigorite and any aluminous, well-crystalline lizardite and suggests the elimination of these materials as a good feedstock candidate. Conversely, any chrysotile, non-aluminous, widely spaced lizardite or disordered serpentine feedstocks can be recommended strongly.

Further, it has been shown that the formation of leaching-induced siliceous layers was not universal and where present, resulted from a combination of incongruent dissolution and re-precipitation of amorphous silica in the secondary micro-porosity, facilitated by the intrinsic microtexture of the particles. Although, the results presented here are based on acid-leaching, they are directly related

Authors version

to the intrinsic mineral properties; hence it is plausible to propose that this study can serve as a generic basis for any acid-based geochemical system including the CCSM pre-treatment.

It is noted that, by far, the most commonly occurring serpentine is lizardite, yet little is still known on the natural variability of lizardite polytype and the composition of most serpentinites. Consequently, it is essential that any serpentinite resource considered as feedstock for CCSM is characterised using complimentary methods to will reveal their detailed mineralogical and chemical composition as well as microtextural arrangements.

Acknowledgements

This research was funded by the British Geological Survey, the University of Nottingham and Caterpillar Inc. Professor M Mellini is thanked for providing a sample of lizardite 1T from Elba, Italy. C. Rochelle, G. Purser and A. Kilpatrick are acknowledged for their support in the hydrothermal laboratories at BGS; J Fletcher and P Neep are thanked for preparation of polished thin sections, whilst M Watts and I Mountaney for facilitating the chemical analyses. M Fay and C Parmenter at the Nottingham Nanotechnology and Nanoscience Centre are acknowledged for their support with the Transmission Electron Microscopy. Two anonymous reviewers are thanked for their comments and suggestions that improved the manuscript. The authors publish with the permission of the Executive Director of the British Geological Survey (NERC).

References

Adler H. H. and P. F. Kerr (1963). Infrared spectra, symmetry and structure relations of some carbonate minerals. The American Mineralogist, 48 (July-August), 839-853.

ASTM International. Standard Guide for quantitative analysis by Energy-Dispersive Spectroscopy, ASTM E1508-12a

Bailey S. W. (1969). Polytypism of trioctahedral 1:1 layer silicates. Clays and Clay Minerals, 17, 355-371.

Baronnet A., M. Mellini and B. Devouard (1994). Sectors in polygonal serpentine - a model based on dislocations. Physics and Chemistry of Minerals, 21(5), 330-343.

Bide T., Styles M.T., and Naden J. (2014). An assessment of global resources of rocks as suitable raw materials for carbon capture and storage by mineralisation, Applied Earth Science, 123 (3), 179-195

Brantley S. L. (2008). “Kinetics of mineral dissolution” in Brantley, S. L., J. D. Kubicki, and A. F. White (2008). Kinetics of water-rock interaction Book, 833 pp., Springer Science Business Media, New York, NY 10013.

Authors version

Capitani G., and M. Mellini (2004). The modulated crystal structure of antigorite: The m=17 polysome, American Mineralogist, 89(1), 147-158.

Caruso L. J., and J. V. Chernosky Jr. (1979). The stability of lizardite, Canadian Mineralogist, 17, 757-769.

Cressey G., B. A. Cressey, and F. J. Wicks (2008). Polyhedral serpentine: a spherical analogue of polygonal serpentine? Mineralogical Magazine, 72(6), 1229-1242.

Cressey G., B. A. Cressey, F. J. Wicks, and K. Yada (2010). A disc with fivefold symmetry: the proposed fundamental seed structure for the formation of chrysotile asbestos fibres, polygonal serpentine fibres and polyhedral lizardite spheres, Mineralogical Magazine, 74(1), 29-37.

Critelli T., Marini L., Schott J., Mavromatis V., Apollaro C., Rinder T., De Rosa R., Oelkers E.H. (2015). Dissolution rates of antigorite from a whole-rock experimental study of serpentinite dissolution from 2 < pH < 9 at 25 °C Implications for carbon mitigation via enhanced serpentinite weathering. *Applied Geochemistry*, 61, 259-271.

Culka A., J. Jehlicka, and I. Nemec (2009). Raman and infrared spectroscopic study of boussingaultite and nickelboussingaultite, Spectrochimica Acta Part a-Molecular and Biomolecular Spectroscopy, 73(3), 420-423.

Daval D., Sissmann, O., Menguy, N., Saldi, G.D., Guyot, F., Corvisier, I. M., Garcia, B., Machouk, I., Knauss, K.G., Hellmann, R. (2011). Influence of amorphous silica layer formation on the dissolution rate of olivine at 90 °C and elevated pCO_2. Chemical Geology 284, 193-209

Daval D., Hellmann, I. Martinez, S. Gangloff, and F. Guyot (2013). Lizardite serpentine dissolution kinetics as a function of pH and temperature, including effects of elevated pCO_2. Chemical Geology 351, 245-256.

Fagerlund J., S. Teir, E. Nduagu, and R. Zevenhoven (2009). Carbonation of magnesium silicate mineral using a pressurised gas/solid process, in Greenhouse Gas Control Technologies 9, edited by J. Gale, H. Herzog and J. Braitsch, pp. 4907-4914.

Farmer V. C. (1974). The layer silicates, in The Infrared Spectra of Minerals, edited, pp. 331-363, The Mineralogical Society London.

Field C. B., et al. (2014). IPCC, Summary for Policymakers. In: Climate Change 2014: Impacts, Adaptation, and Vulnerability. Part A: Global and Sectoral Aspects. Contribution of Working Group II to the Fifth Assessment Report of the Intergovernmental Panel on Climate Change Rep., 32 pp, Cambridge University Press, Cambridge, UK and New York, USA.

Fuchs Y., J. Linares, and M. Mellini (1998). Mossbauer and infrared spectrometry of lizardite-1T from Monte Fico, Elba, Physics and Chemistry of Minerals, 26(2), 111-115.

Gualtieri A. F., C. Giacobbe, and C. Viti (2012). The dehydroxylation of serpentine group minerals, American Mineralogist, 97(4), 666-680.

Authors version

Hellmann R., C. M. Eggleston, M. F. Hochella, and D. A. Crerar (1990). The formation of leached layers on albite surfaces during dissolution under hydrothermal conditions. Geochimica Et Cosmochimica Acta, 54(5), 1267-1281.

Hellmann R., J. M. Penisson, R. L. Hervig, J. H. Thomassin, and M. F. Abrioux (2003). An EFTEM/HRTEM high-resolution study of the near surface of labradorite feldspar altered at acid pH: evidence for interfacial dissolution-reprecipitation, Physics and Chemistry of Minerals, 30(4), 192-197.

Kelemen P. B., and J. Matter (2008). In situ carbonation of peridotite for CO2 storage, Proceedings of the National Academy of Sciences of the United States of America, 105(45), 17295-17300.

Kelemen P. B., J. Matter, E. E. Streit, J. F. Rudge, W. B. Curry, and J. Blusztajn (2011). Rates and Mechanisms of Mineral Carbonation in Peridotite: Natural Processes and Recipes for Enhanced, in situ CO2 Capture and Storage, in Annual Review of Earth and Planetary Sciences, Vol 39, edited by R. Jeanloz and K. H. Freeman, pp. 545-576.

Krevor S. C. M., and K. S. Lackner (2011). Enhancing serpentine dissolution kinetics for mineral carbon dioxide sequestration, International Journal of Greenhouse Gas Control, 5(4), 1073-1080.

Lacinska A. M. (2016) PhD Thesis. Mineralogical and Experimental study of serpentine minerals and ultramafic rocks with application to carbon capture and storage by mineralisation (unpublished).

Lackner K. S., D. P. Butt, and C. H. Wendt (1997). Progress on binding CO_2 in mineral substrates, Energy Conversion and Management, 38, S259-S264.

Larachi F., J. P. Gravel, B. P. A. Grandjean, and G. Beaudoin (2012). Role of steam, hydrogen and pretreatment in chrysotile gas-solid carbonation: Opportunities for pre-combustion CO2 capture, International Journal of Greenhouse Gas Control, 6, 69-76.

Liu Y., A. Wang, and J. J. Freeman (2009). RAMAN, MIR and NIR spectroscopic study of calcium sulfates: gypsum, bassanite and anhydrite, paper presented at 40th Lunar and Planetary Science Conference.

Logvinova A. M., Wirth, R., Sobolev N. V., Seryotkin, Y. V., Yefimova, E. S., Floss, C. and Taylor L. A. (2008). Eskolaite associated with diamond from the Udachnaya kimberlite pipe, Yakutia, Russia. American Mineralogist, 93, 685-690

Madejova J. (2003). FTIR techniques in clay mineral studies, Vibrational Spectroscopy, 31, 1-10.

Maroto-Valer, M. M., M. E. Kuchta, Y. Z. Zhang, J. M. Andresen, and D. J. Fauth (2004). Comparison of physical and chemical activation of serpentine for enhanced Co-2 sequestration, Abstracts of Papers of the American Chemical Society, 227, U1095-U1095.

Matter J. M., and P. B. Kelemen (2009). Enhanced in situ carbonation of peridotite for permanent CO2 storage, Geochimica Et Cosmochimica Acta, 73(13), A848-A848.

McGrail B. P., F. A. Spane, C. R. Amonette, C. R. Thompson and C. F. Brown (2014). Injection and monitoring at the Wallula Basalt Pilot Project, Energy Procedia, 63, 2939-2948.

Authors version

McGrail B. P., H. T. Schaef, A. M. Ho, Y.-J. Chien, J. J. Dooley and C. L. Davidson (2006). Potential for carbon dioxide sequestration in flood basalts, Journal of Geophysical Research-Solid Earth, 111(B12).

Mellini M. (1982). The crystal structure of lizardite 1T - hydrogen bonds and polytypism, American Mineralogist, 67(5-6), 587-598.

Mellini M. and P. F. Zanazzi (1987). Crystal structures of lizardite 1T and lizardite 2H1 from Coli, Italy. American Mineralogist, 72(9-10), 943-948.

Mellini M. and Viti, C (1994). Crystal structure of lizardite-1T from Elba, Italy. American Mineralogist, 79, 1194-1198

Mevel C. (2003). Serpentinization of abyssal peridotites at mid-ocean ridges. Comptes Rendus Geoscience, 335(10-11), 825-852.

Murphy W. M., E. H. Oelkers, and P. C. Lichtner (1989). Surface-reaction versus diffusion control on mineral dissolution and growth-rates in geochemical processes. Chemical Geology, 78(3-4), 357-380.

O'Connor W. K., C. L. Dahlin, D. N. Nilsen, S. J. Gerdemann, G. E. Rush, L. R. Penner, R. P. Walters and P. C. Turner (2002). Continuing studies on direct aqueous mineral carbonation for CO_2 sequestration, in 27th International Technical Conference on Coal Utilisation & Fuel Systems, edited, p. 13, Clearwater, Florida.

O'Hanley D. S., J. V. Chernosky and F. J. Wicks (1989). The stability of lizardite and chrysotile. Canadian Mineralogist, 27, 483-493.

Park A. H. A. and L. S. Fan (2004). CO_2 mineral sequestration: physically activated dissolution of serpentine and pH swing process, Chemical Engineering Science, 59(22-23), 5241-5247.

Parkhurst D. L. and Appelo C. A. J. (1999). User's guide to PHREEQC (Version 2): a computer program for speciation, batch-reaction, one-dimensional transport, and inverse geochemical calculations. Water-Resources Investigation Report. US Geological Survey.

Putnis A. (2009). Mineral replacement reactions, in Reviews in Mineralogy & Geochemistry, edited, pp. 87-124.

Rozalen M. and F.J. Huertas (2013). Comparative effect of chrysotile leaching in nitric, sulphuric and oxalic acids at room temperature. Chemical Geology, 352, 134-142

Ruiz-Agudo E., C. V. Putnis, C. Rodriguez-Navarro and A. Putnis (2012). Mechanism of leached layer formation during chemical weathering of silicate minerals, Geology, 40(10), 947-950.

Ryu K. W., S. C. Chae, and Y. N. Jang (2011). Carbonation of Chrysotile under Subcritical Conditions, Materials Transactions, 52(10), 1983-1988.

Sanna A., A. Lacinska, M. Styles and M. M. Maroto-Valer (2014). Silicate rock dissolution by ammonium bisulphate for pH swing mineral CO_2 sequestration, Fuel Processing Technology, 120, 128-135.

Authors version

Sanna A., X. Wang, A. Lacinska, M. Styles, T. Paulson and M. M. Maroto-Valer (2013). Enhancing Mg extraction from lizardite-rich serpentine for CO_2 mineral sequestration, Minerals Engineering, 49, 135-144.

Schaef H. T., B. P. McGrail, and A. T. Owen (2011). Basalt Reactivity Variability with Reservoir Depth in Supercritical CO_2 and Aqueous Phases, 10th International Conference on Greenhouse Gas Control Technologies, 4, 4977-4984.

Schott J., O. S. Pokrovsky and E. H. Oelkers (2009). The Link Between Mineral Dissolution/Precipitation Kinetics and Solution Chemistry, in Thermodynamics and Kinetics of Water-Rock Interaction, edited by E. H. Oelkers and J. Schott, pp. 207-258.

Schott J., O. S. Pokrovsky, Spalla, O., Devreux, F., Gloter, A. and Mielczarski, J.A. (2012). Formation, growth and transformation of leached layers during silicate minerals dissolution: The example of wollastonite. Geochimica and Cosmochimica Acta, 98, 259-281

Schulze R. K., M. A. Hill, R. D. Field, P. A. Papin, R. J. Hanrahan and D. D. Byler (2004). Characterization of carbonated serpentine using XPS and TEM, Energy Conversion and Management, 45(20), 3169-3179.

Styles M. T., A. Sanna, A. M. Lacinska, J. Naden and M. Maroto-Valer (2014). The variation in composition of ultramafic rocks and the effect on their suitability for the carbon dioxide sequestration by mineralisation following acid leaching, Greenhouse Gas Science and Technology, 4, 1-12.

Teir S., H. Revitzer, S. Eloneva, C.-J. Fogelholm and R. Zevenhoven (2007). Dissolution of natural serpentinite in mineral and organic acids, International Journal of Mineral Processing, 83(1-2), 36-46.

Thom J. G. M., G. M. Dipple, I. M. Power and A. L. Harrison (2013). Chrysotile dissolution rates: Implications for carbon sequestration, Applied Geochemistry, 35, 244-254.

IUPAC 1994. Recommendations for the characterization of porous solids. Pure and Applied Chemistry, 66, 1739-1758

Viti C., and M. Mellini (1997). Contrasting chemical compositions in associated lizardite and chrysotile in veins from Elba, Italy, European Journal of Mineralogy, 9(3), 585-596.

Wang X., and M. M. Maroto-Valer (2011a). Dissolution of serpentine using recyclable ammonium salts for CO2 mineral carbonation, Fuel, 90(3), 1229-1237.

Wang X., and M. M. Maroto-Valer (2011b). Integration of CO_2 Capture and Mineral Carbonation by Using Recyclable Ammonium Salts, Chemsuschem, 4(9), 1291-1300.

Weissbart E. J. and J. D. Rimstidt (2000). Wollastonite: Incongruent dissolution and leached layer formation, Geochimica Et Cosmochimica Acta, 64(23), 4007-4016.

Werner M., S. B. Hariharan, A. V. Bortolan, D. Zingaretti, R. Baciocchi and M. Mazzotti (2013). Carbonation of activated serpentine for direct flue gas mineralization, Energy Procedia, 37, 5929-5937. Proceedings of the 11th International Conference on Greenhouse Gas Control Technologies.

Authors version

Wicks F. J. and E. J. W. Whittaker (1975). A reappraisal of the structures of the serpentine minerals. Canadian Mineralogist, 13, 227-243.

Wolf G. H., A. V. G. Chizmeshya, J. Diefenbacher and M. J. McKelvy (2004). In situ observation of CO_2 sequestration reactions using a novel microreaction system, Environmental Science & Technology, 38(3), 932-936.

Yoo K., B.-S. Kim, M.-S. Kim, J.-c. Lee and J. Jeong (2009). Dissolution of Magnesium from Serpentine Mineral in Sulfuric Acid Solution, Materials Transactions, 50(5), 1225-1230.

Authors version